Cell Reports
Medicine

Article

High-fructose feeding suppresses cold-stimulated brown adipose tissue glucose uptake independently of changes in thermogenesis and the gut microbiome

Graphical abstract

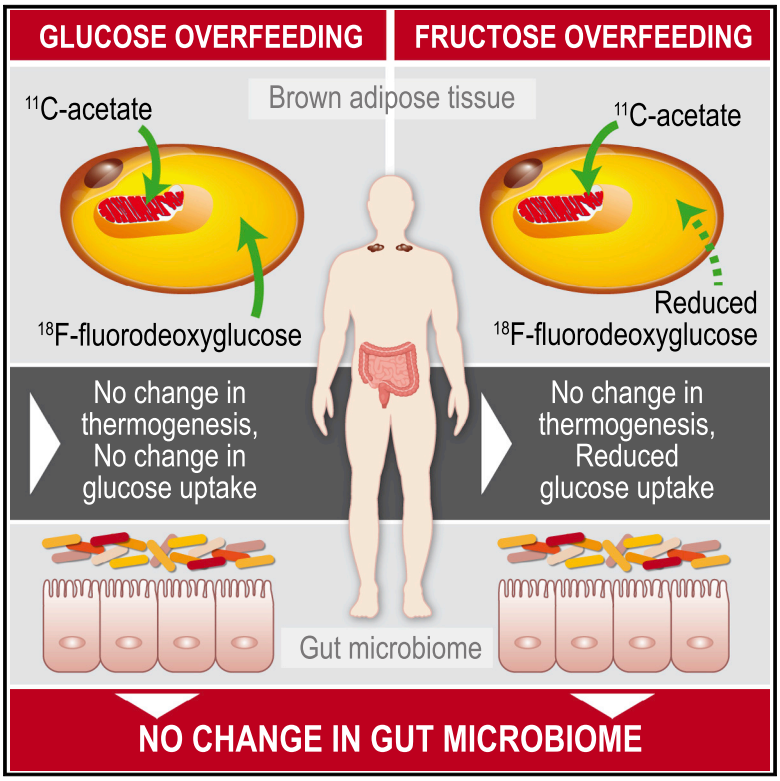

Highlights

- Fructose overfeeding decreases brown adipose tissue glucose metabolism
- These changes occur independently of oxidative metabolism
- No change is observed with glucose overfeeding
- The gut microbiome is not affected by fructose/glucose overfeeding

Authors

Gabriel Richard, Denis P. Blondin, Saad A. Syed, ..., Gregory R. Steinberg, Katherine M. Morrison, André C. Carpentier

Correspondence

Andre.Carpentier@USherbrooke.ca

In brief

Richard et al. show that after 2 weeks of fructose overfeeding, brown adipose tissue (BAT) glucose consumption decreases independently of changes in thermogenesis and gut microbiome. This impairment of BAT function does not occur with glucose overfeeding and is a very early sign of fructose-induced dysmetabolism.

Richard et al., 2022, Cell Reports Medicine *3*, 100742
September 20, 2022
https://doi.org/10.1016/j.xcrm.2022.100742

CellPress

Cell Reports Medicine

CellPress
OPEN ACCESS

Article

High-fructose feeding suppresses cold-stimulated brown adipose tissue glucose uptake independently of changes in thermogenesis and the gut microbiome

Gabriel Richard,[1,2] Denis P. Blondin,[1,3] Saad A. Syed,[4] Laura Rossi,[5] Michelle E. Fontes,[5] Mélanie Fortin,[1] Serge Phoenix,[1,2] Frédérique Frisch,[1] Stéphanie Dubreuil,[1] Brigitte Guérin,[1,2] Éric E. Turcotte,[1,2] Martin Lepage,[1,2] Michael G. Surette,[4,5,6,9] Jonathan D. Schertzer,[4,6,9] Gregory R. Steinberg,[4,6,10] Katherine M. Morrison,[6,7] and André C. Carpentier[1,8,11,*]

[1]Centre de recherche du Centre hospitalier universitaire de Sherbrooke, Sherbrooke, QC J1H 5H3, Canada
[2]Department of Nuclear Medicine and Radiobiology, Faculty of Medicine and Health Sciences, Université de Sherbrooke, Sherbrooke, QC J1H 5H3, Canada
[3]Department of Medicine, Division of Neurology, Faculty of Medicine and Health Sciences, Université de Sherbrooke, Sherbrooke, QC J1H 5H3, Canada
[4]Department of Biochemistry and Biomedical Sciences, McMaster University, Hamilton, ON L8S 4L8, Canada
[5]Department of Medicine, McMaster University, Hamilton, ON L8S 4L8, Canada
[6]Centre for Metabolism, Obesity, and Diabetes Research, McMaster University, Hamilton, ON L8N 3Z5, Canada
[7]Department of Pediatrics, McMaster University, Hamilton, ON L8N 3Z5, Canada
[8]Department of Medicine, Division of Endocrinology, Faculty of Medicine and Health Sciences, Université de Sherbrooke, Sherbrooke, QC J1H 5H3, Canada
[9]Farncombe Family Digestive Health Research Institute, McMaster University, Hamilton, ON L8S 4L8, Canada
[10]Division of Endocrinology and Metabolism, Department of Medicine, McMaster University, Hamilton, ON L8S 4L8, Canada
[11]Lead contact
*Correspondence: Andre.Carpentier@USherbrooke.ca
https://doi.org/10.1016/j.xcrm.2022.100742

SUMMARY

Diets rich in added sugars are associated with metabolic diseases, and studies have shown a link between these pathologies and changes in the microbiome. Given the reported associations in animal models between the microbiome and brown adipose tissue (BAT) function, and the alterations in the microbiome induced by high-glucose or high-fructose diets, we investigated the potential causal link between high-glucose or -fructose diets and BAT dysfunction in humans. Primary outcomes are changes in BAT cold-induced thermogenesis and the fecal microbiome (clinicaltrials.gov, NCT03188835). We show that BAT glucose uptake, but not thermogenesis, is impaired by a high-fructose but not high-glucose diet, in the absence of changes in the gastrointestinal microbiome. We conclude that decreased BAT glucose metabolism occurs earlier than other pathophysiological abnormalities during fructose overconsumption in humans. This is a potential confounding factor for studies relying on ^{18}F-FDG to assess BAT thermogenesis.

INTRODUCTION

The consumption of fructose, a food additive highly prevalent in ultra-processed foods in the form of sucrose or high-fructose corn syrup, has risen precipitously over the past few decades. Its overconsumption has paralleled the rapid rise in obesity and the associated metabolic complications, including insulin resistance, non-alcoholic fatty liver disease, and cardiovascular disease. Animal studies, primarily performed in rodents, have consistently demonstrated that diets high in sucrose or fructose induce hypertriglyceridemia and hyperinsulinemia, providing a causal link between fructose consumption and dysmetabolism.[1–4] Such direct evidence in humans, however, has remained more elusive. Several pivotal short-term intervention studies in humans have shown that consuming fructose-sweetened beverages contributing 10% to 25% of energy intake increases circulating triglyceride levels, visceral adiposity, hepatic lipid accretion, and insulin resistance compared with isocaloric glucose or sweeteners.[5–9] Conversely, restricting sugar-sweetened beverages in children with obesity[10,11] lowered fasting triglyceride levels and hepatic fat, while also improving postprandial insulin kinetics. While these studies have been critical to the characterization of the impact of consuming modest levels of fructose on metabolic risk factors, the mechanisms by which isocaloric fructose may promote metabolic disease and its association with insulin resistance remain unknown. This has been particularly difficult to ascertain given the limited number of studies using appropriate controls and directly comparing the effects of fructose-sweetened beverages with isocaloric glucose.

One emerging mechanism that has been proposed as a driving factor in fructose-induced dysmetabolism is the progressive impairment in brown adipose tissue (BAT) metabolic activity.

Retrospective studies commonly report that high spontaneous BAT activity is associated with a favorable metabolic profile including lower circulating triglycerides and higher insulin sensitivity,[12–15] whereas impairments in BAT glucose uptake, non-esterified fatty acid (NEFA) uptake, blood flow, and insulin sensitivity have been noted in aging, obesity, and type 2 diabetes (T2D).[14,16–18] Although several recent studies have demonstrated the ability to activate human BAT through acute and intermittent cold exposure and acute and chronic beta-adrenergic stimulation,[19–25] our understanding of the factors that suppress its activity with aging, obesity, or T2D remains incomplete. Recent evidence in rodents suggests that fructose ingestion increases intestinal microbiota-derived acetate production, which may not only provide a precursor for hepatic lipogenesis[26] but could incidentally suppress BAT function,[27] providing a prospective causal role for BAT in fructose-associated dysmetabolism.

We hypothesized that fructose could impair BAT metabolic activity and thermogenesis and may be an early feature of the fructose-induced deterioration in metabolic profile in humans. To test this hypothesis, we conducted a randomized crossover 2-week fructose versus glucose overfeeding (+25% of energy intake) study in 10 healthy young men, interspersed by a 4-week washout period and preceded by a metabolic assessment performed under an isocaloric condition. The primary outcomes were (1) changes in the fecal microbiome and short-chain fatty acid (SCFA) composition, and (2) BAT cold-induced thermogenesis, assessed via measures of oxidative metabolism and intracellular triglyceride depletion. Based on previous studies, we expected that fructose would change the taxonomic composition of the microbiome,[28] that fecal acetate would increase,[26] and that BAT oxidative metabolism would decrease.[27] Consequently, the decrease in oxidative metabolism would lead to less BAT intracellular triglyceride depletion during BAT activation. Whole-body energy metabolism and BAT glucose metabolism were also investigated as secondary outcomes. Based on previous studies of pharmacological BAT inhibition, we did not expect to see a detectable change in whole-body heat production, but a significant decrease in BAT oxidative metabolism and glucose uptake was expected.[29] A complete list of the primary and secondary outcomes for this study is available on clinicaltrials.gov (NCT03188835).

RESULTS

Short-term fructose overfeeding does not alter adiposity, the gut microbiome, or fecal SCFAs

The high-fructose and high-glucose diets were designed to be hypercaloric, with the carbohydrate-enriched drink representing an additional 25% of the total caloric intake. Each diet was administered for 2 weeks in an outpatient setting based on previous studies showing effects of this level of high-fructose consumption on plasma lipid profiles.[6,7] The short duration of each diet minimized weight gain and changes in body composition, which are potential confounding factors. Participants confirmed drinking the entire diet supplement and were instructed to keep their other dietary intake the same as in the baseline isocaloric period. Changes in total body mass, fat mass, and lean mass (after the diet versus before the diet) were highly variable between individuals for all diets (Figure 1A). On average, there was no difference in body composition between diets. The high-fructose diet elicited a more reproducible increase in total body weight, although this seemed to be related to a gain in lean body mass, rather than in fat mass. Physical activity levels and resting energy expenditure did not change between diets (Figures 1B and 1C). Similarly, there were no differences in tissue-specific fat content assessed by magnetic resonance imaging (MRI) for BAT, subcutaneous or visceral adipose tissue, or the liver (Figure 1D). These results are coherent with those of Stanhope et al.[5] reporting changes in body weight of less than 0.25 kg per week of diet.

We investigated the effects of the high-carbohydrate diets on the fecal microbiome composition through 16S ribosomal RNA gene variable region 3–4 sequencing. Participants provided stool samples at the end of every 2-week diet period (at baseline, high glucose, and high fructose). No significant differences in fecal microbiome composition were observed in terms of taxonomic composition, α-, and β-diversity (Figures 2A–2C). We also measured the fecal SCFA content (acetate, butyrate, and propionate), important metabolites produced by microbiota fermentation of indigestible carbohydrates, by gas chromatography–tandem mass spectrometry. There was no effect of the diets on SCFA content or content ratios (e.g., acetate/propionate ratio), although there was a high variability between subjects (Figures 2D and 2E). By comparison, large changes in the gut microbiome and SCFA were reported as early as 5 days following the onset of plant-based or animal-based diets.[30]

Cold-induced BAT oxidative metabolism and intracellular triglycerides depletion remain normal after the carbohydrate-enriched diets

Participants underwent mild cold exposure (18°C) to activate BAT metabolism.[31] Primary outcomes were BAT oxidative metabolism assessed with ^{11}C-acetate positron emission tomography (PET), as well as intracellular fatty acid content and composition assessed by MRI and magnetic resonance spectroscopy (MRS).

During the intervention, skin temperature, shivering activity, heat production, circulating energy substrates, whole-body substrate oxidation, and hormones were also measured (Table 1). As expected, cold exposure elicited a decrease in mean skin temperature and increase in heat production, and this was fueled mainly by an increase in fatty acid oxidation. Both blood glucose and insulin levels decreased during cold exposure, while circulating levels of non-esterified fatty acids increased. This is consistent with an increase in glucose uptake by tissues and an increase in whole-body adipose tissue intracellular lipolysis.

The time-activity curves of ^{11}C-acetate in BAT showed a higher uptake and washout during cold exposure than at room temperature (Figure 3A). These changes were quantified with a four-compartment, two-tissue model developed by our group.[32,33] With this model, the uptake parameter (K_1) can be used to estimate blood flow changes because first-pass extraction of the tracer is very high in most tissues.[34] The washout parameter (k_2) represents oxidation (i.e., BAT thermogenesis). There was a significant increase in blood flow (Figure 3C; p =

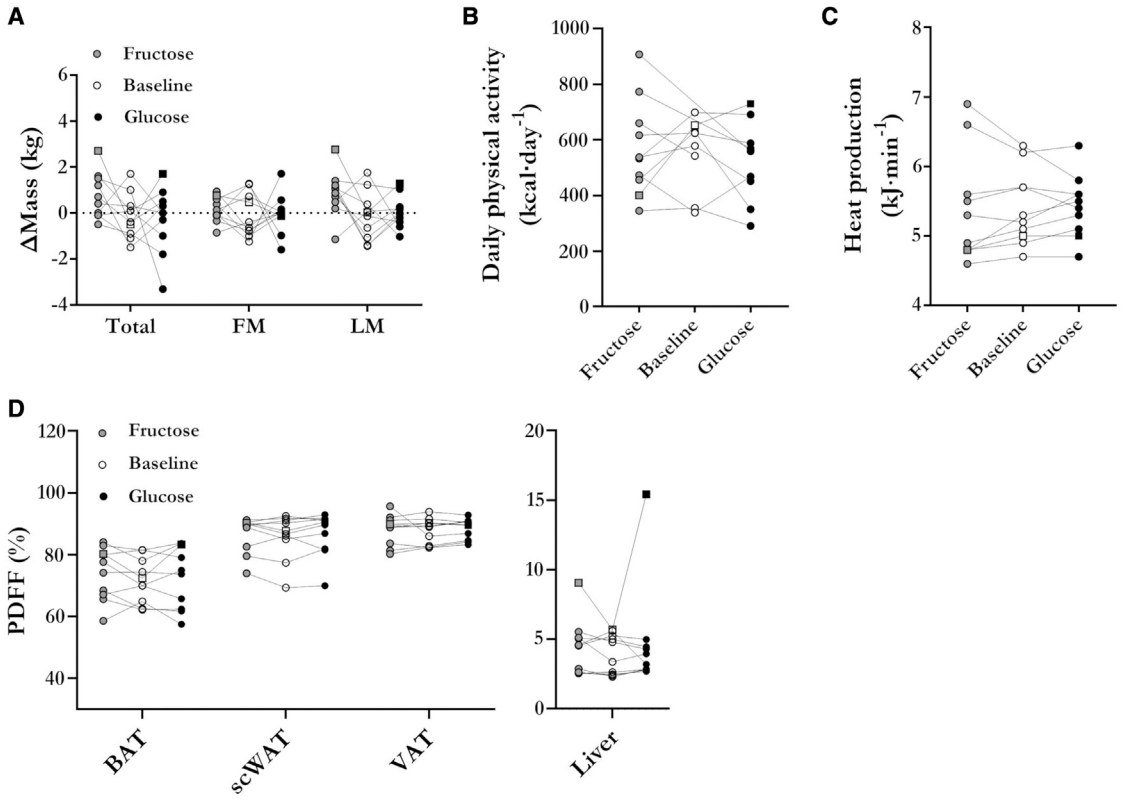

Figure 1. Body composition at baseline and following the high-carbohydrate diets

No significant change in whole-body or tissue-specific composition was noted with the different diets.

(A) Changes in body mass and composition assessed (after the diet - before the diet) by dual-energy X-ray absorptiometry (n = 10).

(B) Energy expenditure from exercise assessed by uniaxial accelerometer at baseline (n = 8), during high fructose consumption (n = 10), and high glucose consumption (n = 9).

(C) Whole-body energy expenditure at rest assessed by indirect calorimetry (n = 10).

(D) Fat content of tissues assessed by Dixon MRI (n = 10). All p values are >0.05. BAT, brown adipose tissue; FM, fat mass; PDFF, proton-density fat fraction; LM, lean mass; scWAT, subcutaneous white adipose tissue; VAT, visceral adipose tissue. Participant 13 was excluded from the analyses due to antibiotic use (potential effects on the microbiome) before the fructose and glucose diets and is shown with a square symbol shape.

0.007) and oxidation (Figure 3D; p = 0.003) during cold exposure, consistent with increased mitochondrial respiration. However, there was no significant difference between diets in blood flow (fructose: p = 0.3; glucose p = 0.5) or oxidation (fructose and glucose: p = 0.6) during cold exposure, suggesting that mitochondrial respiration is not affected by 2 weeks of high-carbohydrate diet. Measures at room temperature were only acquired during the baseline protocol to limit radiation exposure to participants. Therefore, the magnitude of change between room temperature and cold exposure is reported only at baseline.

Intracellular triglyceride content, as assessed by Dixon MRI proton-density fat fraction, decreased in BAT during cold exposure (Figure 3B). The reduction in BAT proton-density fat fraction following cold exposure was consistent with previous studies[35–38] and with the previously reported increase in BAT radiodensity,[29,39–41] which both reflect a progressive decrease in intracellular triglyceride content. This is also consistent with previous findings by our group indicating that intracellular triglycerides are the preferred energy source for BAT thermogenesis.[29] Diets did not modify the BAT proton-density fat fraction at room temperature (Figure 1D) nor the shift with cold exposure (Figure 3B). These findings are in line with the previous observations that diets did not alter body composition, and that BAT oxidative metabolism was preserved.

Furthermore, the lipid composition of BAT and subcutaneous white adipose tissue investigated by MRS (Table 2) were not affected by diets or cold exposure. However, as expected,[42] BAT contained more saturated fatty acids than subcutaneous white adipose tissue, demonstrated by a lower number of double bonds (median for all diets and temperatures: 3.5 [IQR: 3.0–3.8] versus 4.1 [IQR: 3.4–4.5]; p = 0.002) and methylene-interrupted single bonds (median for all diets and temperatures: 1.4 [IQR: 1.0–2.0] versus 3.3 [IQR: 2.6–3.9]; p < 0.0001).

Short-term fructose overfeeding reduces BAT glucose uptake

Tissue-specific glucose metabolism was assessed by ^{18}F-fluorodeoxyglycose (^{18}F-FDG) PET during cold exposure. The time-activity curves of ^{18}F-FDG in BAT (Figure 4A) show a quick initial increase in signal, corresponding to the first-pass extraction of

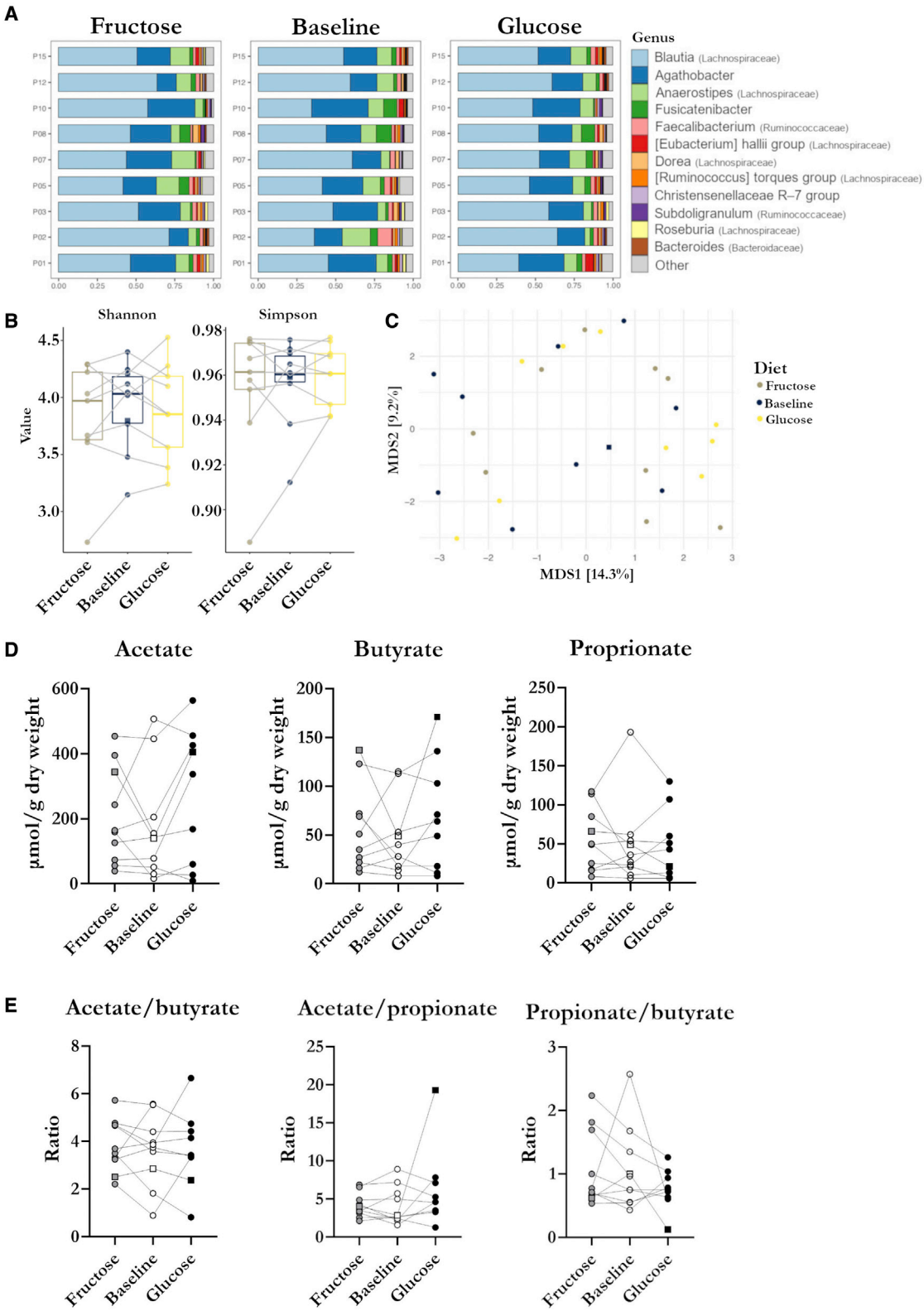

(legend on next page)

^{18}F-FDG by the tissue. Afterward, the signal continues to increase at a slower pace as ^{18}F-FDG in the blood is taken up and trapped into BAT. The initial uptake phase appears similar for all diets. However, the subsequent trapping rate of ^{18}F-FDG is slower after the high-fructose diet. To quantify this phenomenon, BAT fractional glucose uptake was assessed with a Patlak graphical model.[43] The tissue metabolic rate of glucose was then calculated using fractional glucose extraction, glucose concentration, and a lumped constant of 1.14 for fat and 1.16 for muscle.[44,45] Both the fractional extraction (Figure 4B; $p = 0.044$) and metabolic rate of glucose (Figure 4C; $p = 0.036$) decreased in BAT following the high-fructose diet, but not following the high-glucose diet. We did similar measures and modeling in different skeletal muscles as well as subcutaneous adipose tissue and conclude that this decrease in glucose uptake was specific to BAT (Figure 4D). The reduction in cold-stimulated BAT glucose uptake following the high-fructose diet was not associated with differences in blood glucose, insulin, homeostatic model assessment for insulin resistance (HOMA-IR), glucagon, cortisol, c-peptide, glucose-dependent insulinotropic polypeptide, or glucagon-like peptide-1. Furthermore, no difference in whole-body carbohydrate oxidation was observed with diets (Table 1).

These observations point to a very localized reduction in glucose uptake specific to BAT and independent of changes in oxidative metabolism or intracellular triglyceride depletion. Because ^{18}F-FDG PET provides macroscopic data (with 4 mm^3 image voxels) and does not discriminate between metabolic pools (i.e., ^{18}F-FDG and ^{18}F-FDG-6-phosphate produce the same signal), we cannot determine the exact cause of this reduced uptake. Based on the ^{11}C-acetate data, blood flow is not affected by the fructose diet. Therefore, the reduction in glucose uptake is likely due to a deficit in transport into the brown adipocytes (e.g., fewer glucose transporters or reduced transporter activity), reduced phosphorylation rates, or a combination of both. Whether this is related to a local effect of circulating acetate, as suggested by Sun et al.,[27] cannot be determined with our experimental design. There was no change in the acetate content of the stool samples, and plasma acetate could not be measured accurately by our gas chromatography–tandem mass spectrometry method.

Fructose overfeeding increases liver triglyceride content as well as serum VLDL-TG in the cold

The liver triglyceride content assessed by MRI was significantly increased after cold exposure compared with room temperature only after the high-fructose diet (Figure 5A and Table 2; $p = 0.037$). This increase was not observed in the neighboring visceral or subcutaneous adipose tissues (Figure 5A), and as noted previously, BAT triglyceride content decreased in the cold exposure condition (Figure 3B). This suggests that fructose consumption promotes hepatic lipid storage under cold-induced increase in adipose tissue intracellular lipolysis, even though the magnitude of this increased lipolysis is not affected by diets (Figures 5B and 5C).

We also measured circulating very low-density lipoprotein-triglycerides (VLDL-TG), which are secreted by the liver.[46] An increase in *de novo* lipogenesis due to excess glucose, and especially, fructose has been linked to increased liver fat content and circulating VLDL-TG.[47,48] We did observe a trend toward elevated VLDL-TG with the carbohydrate-supplemented diets compared with isocaloric diet, but this increase was only significant during cold exposure (Figure 5D; fructose: $p = 0.023$; glucose: $p = 0.013$). Whether this is caused by increased production of VLDL-TG by the liver or by reduced tissue clearance cannot be determined with the current data.

The possible link between changes in whole-body lipolysis and lipogenesis in the liver and BAT metabolism requires further investigation. There was no correlation between baseline liver triglyceride content, or cold-induced changes in BAT triglyceride content, and BAT glucose uptake or oxidative metabolism. However, if there was an increase in VLDL-TG secretion by the liver, it could serve as an alternative energy substrate for BAT instead of glucose. Indeed, we have previously shown a direct competition between the uptake of triglyceride-rich lipoprotein-derived fatty acids and circulating glucose, with the former reducing BAT glucose uptake by more than 50% in the postprandial state.[49]

DISCUSSION

Over the past decades, there has been a significant shift in our food supply system that was accompanied by the addition of food additives such as fructose. These changes have paralleled the rise in obesity and its associated metabolic complications. This study aimed to examine whether 2-week overconsumption of fructose could modify the gut microbiome and the production of SCFA, especially acetate, and elicit changes in BAT metabolism. None of the diets, supplemented with either glucose or fructose for 2 weeks, had any effect on body composition, BAT composition, the gastrointestinal microbiome, or fecal SCFA levels. Although fructose overconsumption did not change

Figure 2. Fecal microbiome analyses and fecal short-chain fatty acids for the different diets

(A) Relative abundance taxonomic summaries divided by diet and ordered by participant for all participants included in statistical analyses (n = 9). Top 12 genera in the data were colored and are identified in the legend. All other genera are in "other."

(B) Participants' fecal microbial α-diversity assessed by Shannon and Simpson indices at baseline (n = 10), following high fructose consumption (n = 9) and high glucose consumption (n = 9). Each dot represents the value of the diversity metric from each sample. The boxes show the median and interquartile range. A generalized mixed-effects model found no significant differences by α-diversity.

(C) Participants' fecal microbial β-diversity assessed by Aitchison distance and visualized using a Principal-Coordinate Analysis plot. Each dot represents a sample and samples are colored by diet (baseline [n = 10], high fructose [n = 9], and high glucose [n = 9]). A permutational multivariate ANOVA found no significant differences by β-diversity. Percent variation explained by each axis is noted in square brackets.

(D) Fecal short-chain fatty acid composition for baseline (n = 10), high fructose (n = 10), and high glucose (n = 9). No significant difference was observed between diets.

(E) Fecal short-chain fatty acid ratios. No significant difference was observed between diets. All p values are >0.05. Participant 13 was excluded from the analyses due to antibiotic use (potential effects on the microbiome) before the fructose and glucose diets and is shown with a square symbol shape.

Table 1. Whole-body response to diets and cold

	Baseline		Fructose		Glucose	
	RT	18°C	RT	18°C	RT	18°C
EE ($kJ \cdot min^{-1}$)	5.5 (5.0–5.9)	8.5 (7.2–9.9)[d]	5.4 (4.8–6.1)	8.7 (7.7–9.6)[d]	5.5 [5.1–5.8]	8.7 (7.4–9.9)[d]
Skin temperature (°C)	34.5 (33.8–35.2)	28.6 (27.9–29.4)[d]	34.2 (33.8–34.7)	29.0 (28.0–30.0)[d]	34.4 (33.9–35.0)	28.6 (27.8–29.3)[d]
Shivering intensity (%MVC)[f]	Not measured at RT	1.29 (0.69–1.88)	Not measured at RT	1.50 (0.72–2.28)	Not measured at RT	1.43 (0.71–2.15)
$R_{aGlucose}$ ($\mu mol \cdot min^{-1}$)	1902 [1642–2227]	1457 [1332–1492][d]	2134 (1716–2552)	1529 (1163–1894)[d]	1989 (1710–2269)	1553 (1334–1772)[d]
R_{aNEFA} ($\mu mol \cdot min^{-1}$)	540 (311–770)	1195 (765–1626)[b]	657 (374–940)	1132 (732–1532)[a]	849 (435–1263)	1430 (879–1982)[a]
$R_{aGlycerol}$ ($\mu mol \cdot min^{-1}$)	276 [195–334]	859 [758–1431][b]	305 [254–369]	941 [589–2302][c]	327 [219–396]	986 [725–1647][b]
Glucose (mmol/L)	4.9 (4.7–5.1)	4.6 (4.2–5.0)[a]	4.8 [4.7–5.0]	4.5 [4.3–4.8][b]	4.5 [4.4–5.1]	4.6 [4.1–4.9][a]
Insulin (pmol/L)	60.7 (43.9–77.6)	38.6 (27.1–50.1)[b]	53.9 (37.3–70.4)	40.5 (32.2–48.7)	55.8 (36.1–75.5)	39.7 (25.4–53.9)
Glucagon ($pg \cdot mL^{-1}$)	55.3 (25.9–84.8)	46.4 (24.5–68.3)	48.9 (26.0–71.7)	40.9 (19.6–62.1)	59.7 (24.5–94.9)	48.3 (18.7–77.8)
TG (mmol/L)	0.60 [0.43–1.34]	0.60 [0.46–1.54]	0.63 [0.49–1.60]	0.68 [0.43–1.58]	1.14 (0.47–1.81)	1.02 (0.50–1.54)
VLDL-TG (mmol/L)	0.24 [0.14–0.40]	0.15 [0.11–0.29]	0.32 (0.15–0.49)	0.36 (0.14–0.59)[e]	0.36 (0.23–0.49)	0.38 (0.18–0.57)[e]
NEFA (μmol/L)	290 (164–416)	612 (389–836)[b]	321 (190–452)	538 (377–699)[b]	316 (177–454)	558 (405–711)[c]
TSH ($IU \cdot L^{-1}$)	1.9 (1.1–2.6)	1.5 (0.9–2.2)[a]	1.8 (1.1–2.6)	1.4 (0.8–2.0)[b]	1.6 (1.1–2.1)	1.4 (0.9–1.9)
Free T3 (pmol/L)	5.2 (4.9–5.6)	5.4 (4.8–5.9)	5.7 [5.2–6.2][e]	5.8 [5.1–6.3]	5.5 [5.1–6.1]	5.5 [5.2–6.3]
Free T4 (pmol/L)	17.1 (14.0–20.2)	18.1 (14.6–21.6)	16.6 (15.1–18.0)	17.7 (16.0–19.5)[a]	15.5 [15.1–16.9]	16.3 [15.7–17.5][a]
Cortisol (nmol/L)	230 (201–259)	201 (168–234)	219 (162–276)	230 (195–264)	223 (139–307)	223 (196–251)[e]
Leptin ($ng \cdot mL^{-1}$)	0.8 [0.5–1.8]	0.6 [0.3–1.3][b]	1.4 [0.4–1.9]	0.9 [0.3–1.5][b]	1.2 [0.4–2.0]	0.7 [0.3–1.4][b]
C-peptide (nmol/L)	0.25 (0.18–0.31)	0.18 (0.14–0.22)[b]	0.24 (0.18–0.29)	0.18 (0.14–0.22)[c]	0.21 (0.16–0.26)	0.16 (0.12–0.20)[b]
GIP (pmol/L)	5.4 [4.4–14.4]	7.4 [5.1–9.0]	9.5 (5.7–13.3)	9.1 (6.8–11.3)[e]	8.5 (5.0–11.9)	7.6 (5.2–10.0)
Total GLP-1 (pmol/L)	35.3 (27.3–43.3)	34.4 (26.2–42.5)	32.9 (24.2–41.6)	33.2 (24.4–42.0)	35.2 (25.6–44.9)	35.6 (26.7–44.4)
HOMA-IR	1.91 (1.36–2.45)	1.15 (0.75–1.55)[b]	1.73 (1.15–2.30)	1.20 (0.93–1.47)[a]	1.75 (1.05–2.45)	1.15 (0.72–1.57)

Values are mean (95% confidence interval) for normally distributed data, and median [interquartile range] for nonparametric data. %MVC, percent of maximum voluntary contraction; EE, energy expenditure; GIP, glucose-dependent insulinotropic polypeptide; GLP-1, glucagon-like peptide-1; HOMA-IR, homeostatic model assessment for insulin resistance; NEFA, non-esterified fatty acids; R_a, appearance rate; RT, room temperature; T3, triiodothyronine; T4, thyroxine; TG, triglycerides; TSH, thyroid stimulating hormone; VLDL, very low-density lipoproteins; GIP, glucose-dependent insulinotropic polypeptide; GLP-1, glucagon-like peptide-1; HOMA-IR, homeostatic model assessment for insulin resistance. Participant 13 was excluded from the analyses and is not included in the mean/median calculations due to antibiotic use (potential effects on the microbiome) before the fructose and glucose diets.

Two-way repeated measures ANOVA or repeated measures mixed-effects model with Bonferroni correction for multiple comparisons.

[a]Effect of cold intervention, $p < 0.05$.

[b]$p < 0.01$.

[c]$p < 0.001$.

[d]$p < 0.0001$.

[e]Different from baseline diet, $p < 0.05$.

[f]Shivering data were not collected for participant 15 due to COVID-19 restrictions.

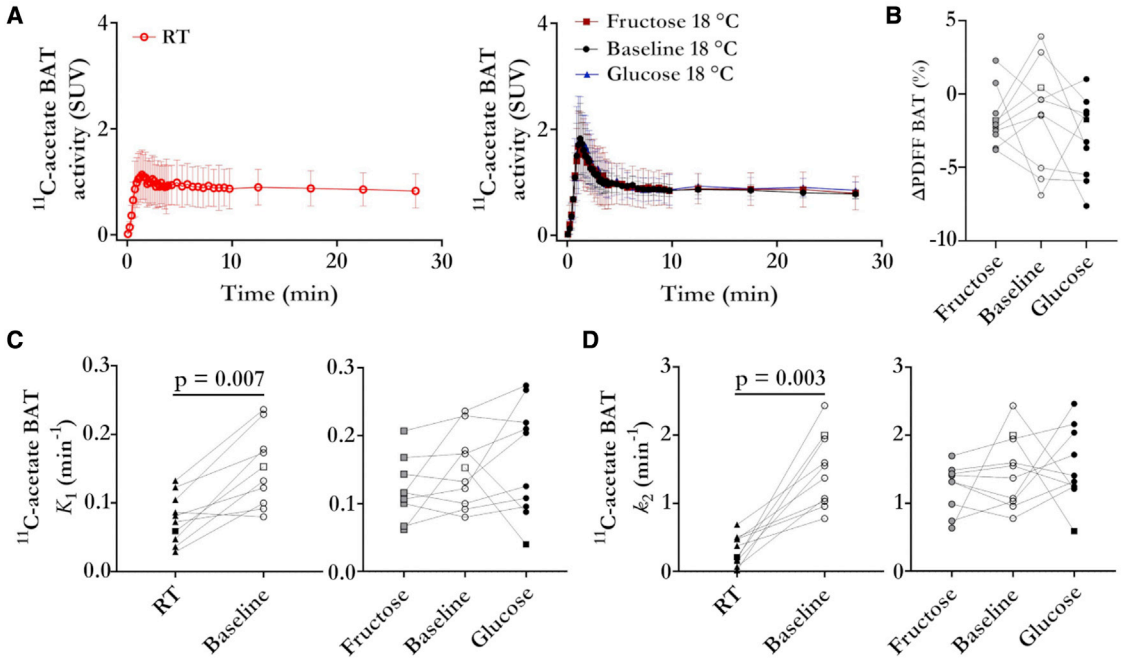

Figure 3. Brown adipose tissue oxidative metabolism and intracellular triglyceride depletion

(A) Mean time-activity curves (with standard deviation) showing the uptake and elimination of ^{11}C-acetate or its metabolites at room temperature (baseline) and during cold exposure (18°C) for baseline, fructose, and glucose diets.

(B) Proton-density fat fraction shift in brown adipose tissue with cold exposure (18°C - room temperature) for the different diets (n = 10). There is no difference in shifts between diets.

(C) Blood flow index at baseline (n = 10; room temperature and cold), high fructose (cold: n = 9), and high glucose (cold: n = 10). A repeated measures mixed-effects model found a significant difference between room temperature and cold exposure (all conditions).

(D) Oxidative metabolism at baseline (n = 10; room temperature and cold), high fructose (cold: n = 9), and high glucose (cold: n = 10). A repeated measures mixed-effects model found a significant difference between room temperature and cold exposure (all conditions). p values are shown only for significant differences (i.e., $p < 0.05$). BAT, brown adipose tissue; PDFF, proton-density fat fraction; K_1, ^{11}C-acetate uptake rate; k_2, ^{11}C-acetate oxidation rate; RT, room temperature; SUV, standardized uptake value. Participant 13 was excluded from the analyses due to antibiotic use (potential effects on the microbiome) before the fructose and glucose diets and is shown with a square symbol shape. ^{11}C-acetate was not performed for participant 13 fructose due to problems with tracer synthesis.

cold-induced BAT oxidative metabolism or the depletion of intracellular triglycerides, it significantly reduced BAT glucose uptake. Interestingly, this BAT metabolic disturbance occurred without any significant changes in tissue blood flow or systemic insulin resistance. Our findings demonstrate that reduced BAT glucose uptake occurs very early after the onset of a high-fructose diet in young and otherwise healthy participants.

We found BAT glucose metabolism to be very sensitive to fructose overconsumption, with BAT metabolic rate of glucose decreasing by 43% (38% decrease in fractional glucose extraction) within 2 weeks of fructose overfeeding. The exact cause of this reduction in BAT glucose uptake remains unclear. Increased caloric intake alone is unlikely to have caused this BAT metabolic abnormality, as consuming glucose did not change BAT glucose uptake. Neither the glucose nor the fructose-supplemented diet affected whole-body insulin sensitivity based on the HOMA-IR, suggesting that the decreased uptake of glucose by BAT precedes whole-body insulin resistance during the development of fructose-induced metabolic dysfunction. BAT samples were not taken during this study, making it impossible to investigate changes in cell morphology or function, which may explain the decrease in glucose uptake.

The combined reduction of BAT glucose uptake with preserved BAT oxidative metabolism and intracellular triglyceride mobilization during cold exposure observed with fructose overfeeding in the healthy participants is reminiscent of our previous observation in cold-exposed individuals with T2D.[16] Thus, 2 weeks of fructose overfeeding provides another example of the uncoupling of BAT oxidative metabolism and glucose uptake.[29,50,51] Our results highlight once again the limitations of ^{18}F-FDG PET as a marker of BAT thermogenesis. Based on these results, the possible effect of diets should be considered in future studies assessing BAT function with ^{18}F-FDG.

Since we do not currently have a reliable non-invasive method of measuring active BAT volume in humans independent of ^{18}F-FDG PET,[52] we cannot determine if the impairment in glucose metabolism is accompanied by a reduction in BAT mass. For this reason, changes in the contribution of BAT to whole-body thermogenesis and glucose clearance cannot be assessed. However, we did not observe an effect of fructose overfeeding on whole-body energy expenditure, suggesting that, if there was a decrease in BAT activity, it was compensated by other thermogenic processes or it was too small to measure.

Table 2. Fat composition of different tissues assessed by MRI and MRS

	Baseline		Fructose		Glucose	
	RT	18°C	RT	18°C	RT	18°C
BAT PDFF (%)	71.8 (66.6–76.9)	70.3 (64.3–76.4)	73.2 (66.5–79.9)	71.5 (63.7–79.3)[a]	71.4 (63.8–79.0)	68.3 (60.0–76.6)[a]
scWAT PDFF (%)	87.2 [83.1–91.2]	88.3 [81.4–91.2]	89.4 [81.1–90.2]	89.6 [80.9–90.9]	89.7 [81.7–91.6]	89.9 [82.9–90.5]
VAT PDFF (%)	87.8 (84.8–90.7)	87.9 (85.5–90.3)	87.9 (83.9–91.9)	88.2 (85.2–91.1)	88.2 (85.5–90.9)	87.0 (83.2–90.8)
Liver PDFF (%)	4.1 [2.5–5.3]	4.5 [2.4–5.3]	4.5 [2.6–5.1]	5.1 [2.8–6.1][a]	3.6 (2.9–4.2)	3.5 (2.6–4.4)
BAT ndb	3.6 (2.5–4.7)	3.9 (3.1–4.6)	3.7 (2.7–4.7)	3.1 (2.6–3.6)	3.6 (2.7–4.5)	3.2 (2.8–3.7)
scWAT ndb	4.1 (3.0–5.2)	3.5 (2.7–4.2)	3.9 (3.2–4.5)	4.1 (3.4–4.8)	4.2 (3.4–5.1)	3.7 (3.0–4.5)
BAT nmidb	2.5 [1.7–3.4]	2.5 [2.2–3.2]	2.2 [1.8–3.3]	2.0 [0.4–2.8]	3.2 (1.7–4.7)	2.0 (1.4–2.6)
scWAT nmidb	3.5 (2.3–4.6)	3.2 (2.6–3.8)	3.2 (2.0–4.3)	2.9 (2.1–3.7)	3.9 (2.9–5.0)	2.4 (1.4–3.5)

Values are mean (95% confidence interval) for normally distributed data, and median [interquartile range] for nonparametric data. BAT, brown adipose tissue; PDFF, proton-density fat fraction; ndb, number of double bonds; nmidb, number of methylene-interrupted double bonds; RT, room temperature; scWAT, lower back subcutaneous white adipose tissue; VAT, visceral adipose tissue. Participant 13 was excluded from the analyses and is not included in the mean/median calculations due to antibiotic use (potential effects on the microbiome) before the fructose and glucose diets.
Two-way repeated measures ANOVA or repeated measures mixed-effects model with Bonferroni correction for multiple comparisons.
[a]Effect of cold intervention, $p < 0.05$.

Finally, in parallel with the impairment of BAT glucose metabolism by fructose, we observed early signs of hepatic dysmetabolism with the carbohydrate-supplemented diets, and especially with high fructose. These early changes included increased lipid storage and circulating VLDL-TG levels, both early characteristic features in the development of fructose-induced fatty liver disease.[47] Interestingly, these effects only emerged under cold stress, as the high-glucose or -fructose diet did not affect hepatic lipid content or VLDL-TG levels at room temperature. The high adipose tissue intracellular triglyceride lipolytic rate stimulated in response to cold exposure resulting in increased circulating NEFA flux likely exacerbated the impact of increased hepatic *de novo* lipogenesis, and possibly reduced fatty acid oxidation that may have been induced by the high-fructose diet.[53,54] It is also possible that the changes in hepatic lipid content are linked to modifications of bile acids composition in the gut or in the circulation.[55,56] Quantification of bile acids should be part of future studies to investigate this mechanism and its possible interactions with BAT thermogenesis.

The possible link between liver and BAT impairment by fructose warrants further investigation. Notably, the increase in circulating VLDL-TG may be involved in a shift in BAT energy substrate consumption from glucose to lipids. However, this shift was not observed with the high-glucose diet despite a similar increase in circulating VLDL-TG. Therefore, if a change of energy substrate occurred, it must have been driven by other factors than just an increase in circulating lipids. Possible mechanisms include early development of insulin resistance in BAT and alterations in adrenergically mediated synthesis or translocation of the glucose transporter, GLUT1.[57] Although peripheral blood fructose levels are generally low, a direct effect of fructose on brown adipocytes is also possible, for example, via an increase in glucose 6-phosphate production, which could limit ^{18}F-FDG uptake through feedback inhibition on hexokinase.[58] Further studies on BAT tissue samples and cell lines will be required to elucidate these mechanisms. Despite its apparent importance in fueling BAT thermogenesis in rodents,[59–61] the role of BAT lipid uptake to fuel thermogenesis in humans appears to be less prominent.[16,31,62,63] More studies are needed to document the role of change in BAT lipid metabolism in the development of metabolic dysfunction in humans.[52]

Limitations of the study

The small sample size of our cohort is the main limitation of this study. The number of participants was voluntarily limited due to time constraints and the high cost of imaging studies. Recruitment was also difficult because of the demands placed on participants (e.g., following diets and undergoing three long and complex imaging visits). For these reasons, of the 16 participants recruited, only 10 participants completed the study. The initial sample size calculation (see STAR Methods) assumed larger changes in oxidative metabolism than those observed in this study. Therefore, if there were small effects of the diets on the microbiome or other outcomes, they could not be detected. Despite the small number of participants, we nevertheless demonstrated the reduction in BAT glucose uptake with fructose overfeeding without any detectable trend toward a reduction in BAT thermogenic activity. The exclusion of one subject who underwent antibiotic treatment during his participation in the study (participant 13) from the analyses did not change the results of this study.

Compliance with the diets is another possible limitation of this study. Participants were not required to fill out daily food diaries, and we thus relied on participants maintaining the same baseline diet throughout the study. However, some participants reported a loss of appetite because of the large quantities of added fructose or glucose or the large volume of beverage supplement consumed (1–1.5 L divided over three separate meals). This may have resulted in the consumption of smaller meals during fructose and glucose overfeeding, thus limiting the intended increase in caloric intake. Also, the supplementation with high quantities of glucose or fructose was designed to maximize potential effects on the microbiome, BAT, and whole-body metabolism during a short 2-week period. This is not representative of normal dietary habits in which smaller quantities[64,65] of added sugar (generally a combination of glucose and fructose) are consumed over long periods of time.

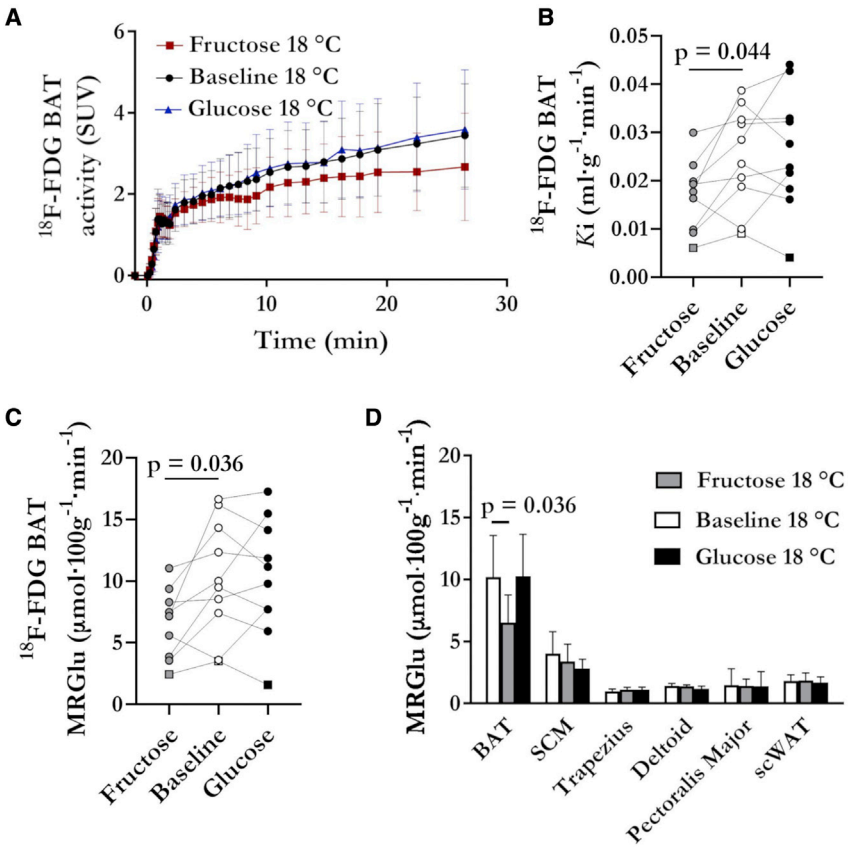

Figure 4. Glucose metabolism of tissues with cold exposure

(A) Mean brown adipose tissue time-activity curves (with standard deviation) showing ^{18}F-fluorodeoxyglucose uptake during cold exposure (18°C) for baseline, fructose, and glucose diets.

(B) Brown adipose tissue fractional glucose uptake at baseline (cold: n = 10), high fructose (cold: n = 9), and high glucose (cold: n = 10). A repeated measures mixed-effects model found a significant difference between baseline and fructose.

(C) Brown adipose tissue metabolic rate of glucose at baseline (cold: n = 10), high fructose (cold: n = 9), and high glucose (cold: n = 10). A repeated measures mixed-effects model found a significant difference between baseline and fructose.

(D) Metabolic rate of glucose for brown adipose tissue compared with skeletal muscles and subcutaneous fat at baseline (cold: n = 10), high fructose (cold: n = 9), and high glucose (cold: n = 10). Data are shown as mean and 95% confidence interval. There was no significant difference for tissues other than BAT (repeated measures mixed-effects model baseline versus fructose). p values are shown only for significant differences (i.e., $p < 0.05$). ^{18}F-FDG, ^{18}F-fluorodeoxyglycose; BAT, brown adipose tissue; K_i, fractional glucose uptake; MRGlu, metabolic rate of glucose; SCM, sternocleidomastoid muscle; scWAT, lower back subcutaneous white adipose tissue; SUV, standardized uptake value. Participant 13 was excluded from the analyses due to antibiotic use (potential effects on the microbiome) before the fructose and glucose diets and is shown with a square symbol shape. Participant 2 fructose ^{18}F-fluorodeoxyglucose was excluded due to excessive participant motion.

However, this study also includes several important strengths, including the crossover design that controlled for inter-individual variation in baseline characteristics and possible lifestyle differences, the use of a 2-week isocaloric control condition performed before the fructose/glucose conditions, and the direct comparison between the overconsumption of fructose and glucose.

Conclusion

Two-week fructose overfeeding did not elicit detectable changes in the microbiome or BAT thermogenesis, but impaired BAT glucose uptake, promoted liver fat storage, and increased circulating VLDL-TG levels during cold exposure in healthy young men. Although the cause and clinical significance of this reduction in BAT glucose metabolism are unclear, our study rules out the potential role of changes in the gut microbiome or the production of SCFAs. It also reveals that reduction in BAT glucose uptake is a very early feature of fructose-induced metabolic disturbance in humans. Its early occurrence in young and otherwise healthy participants makes it a potential confounding factor for studies relying on ^{18}F-FDG to measure changes in BAT thermogenic activity.

STAR★METHODS

Detailed methods are provided in the online version of this paper and include the following:

- KEY RESOURCES TABLE
- RESOURCE AVAILABILITY
  - Lead contact
  - Materials availability
  - Data and code availability
- EXPERIMENTAL MODEL AND SUBJECT DETAILS
  - Human subjects
- METHOD DETAILS
  - Study design
  - Measures of body composition and energy expenditure
  - Diets
  - Stool sample collection and analysis
  - BAT stimulation by cold exposure
  - Energy substrate turnover
  - Imaging of triglyceride content by magnetic resonance imaging
  - Imaging of glucose metabolism and oxidative metabolism by PET/CT
  - Image processing
  - Biological assays
- QUANTIFICATION AND STATISTICAL ANALYSIS
  - Sample size calculation
  - Statistical analysis
- ADDITIONAL RESOURCES

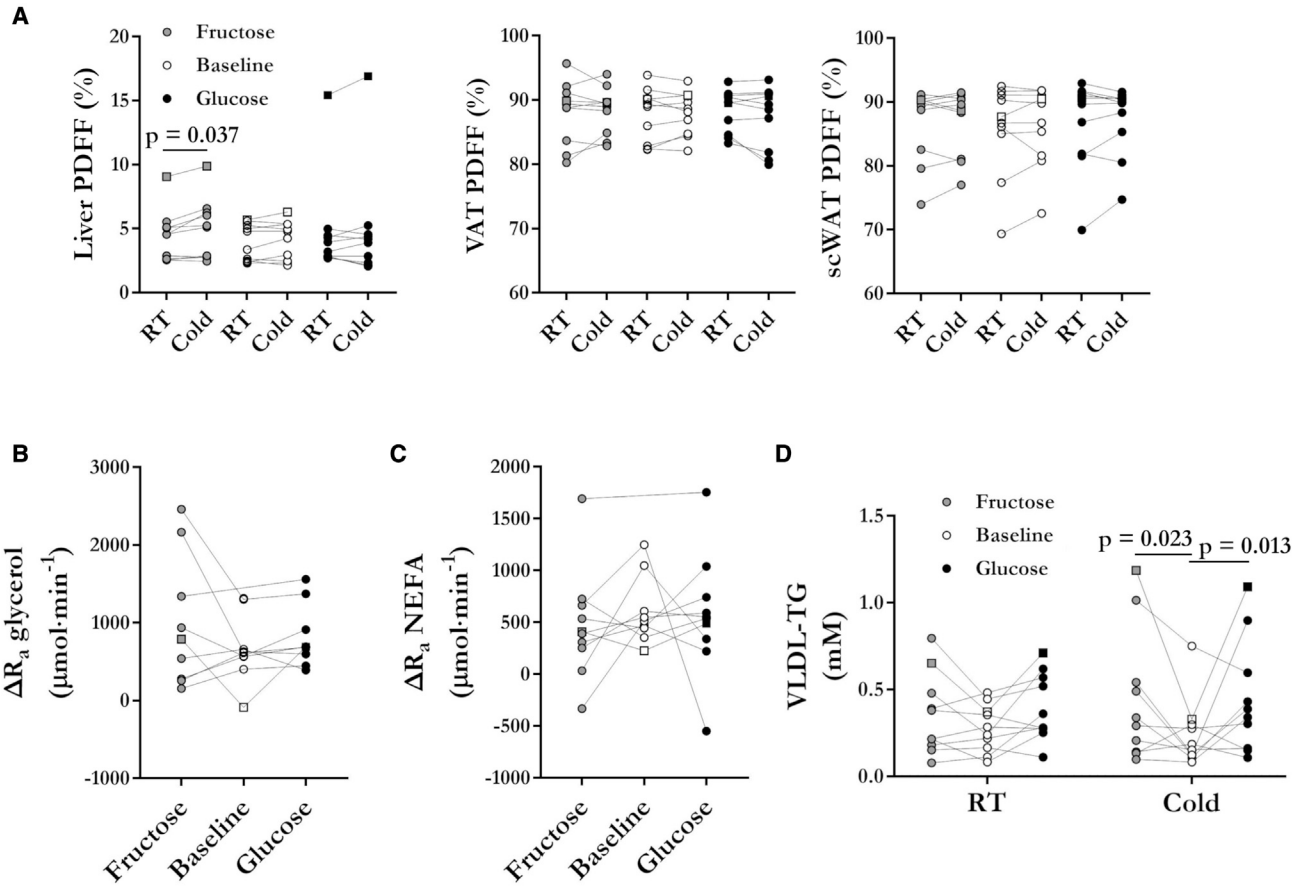

Figure 5. Effect of cold exposure on the liver and whole-body lipid metabolism

(A) Proton-density fat fraction of the liver, visceral adipose tissue, and white adipose tissue at room temperature and in the cold (18°C) for each diet (n = 10). A two-way repeated measures ANOVA found a significant difference between room temperature and cold in the liver with fructose.

(B) Changes in the rate of appearance of glycerol with cold exposure assessed by stable isotope dilution (n = 9).

(C) Changes in the rate of appearance of non-esterified fatty acids with cold exposure assessed by stable isotope dilution at baseline (n = 9), high fructose (n = 10), and high glucose (n = 10).

(D) Circulating very-low-density lipoprotein-triglycerides at room temperature and during cold (n = 10). A two-way repeated measures ANOVA found a significant difference between the baseline and high-carbohydrate diets in the cold. p values are shown only for significant differences (i.e., $p < 0.05$). PDFF, proton-density fat fraction; NEFA, non-esterified fatty acids; R_a, rate of appearance; RT, room temperature; scWAT, subcutaneous white adipose tissue; VAT, visceral adipose tissue; VLDL-TG, very-low-density lipoprotein-triglycerides. Participant 13 was excluded from the analyses due to antibiotic use (potential effects on the microbiome) before the fructose and glucose diets and is shown with a square symbol shape.

SUPPLEMENTAL INFORMATION

Supplemental information can be found online at https://doi.org/10.1016/j.xcrm.2022.100742.

ACKNOWLEDGMENTS

The authors thank Caroll-Lynn Thibodeau, Maude Gérard, Éric Lavallée, Etienne Croteau, Esteban Espinosa, Jean-Philippe Pelletier, Luc Tremblay, Guillaume Gilbert, Christophe Noll, Lucie Bouffard, Zaccary Corradini-Carriere, and all the MR technologists involved in this study for their excellent technical assistance. They also thank the staff of the Farncombe Metagenomic Facility (Hamilton, CA) for support in library sequencing. They also thank Réjean Lebel for his help revising this manuscript. This work was supported by the Canadian Institutes of Health Research (grant number 144625-1, 299962, and PJT 159758). G.R. is a recipient of an NSERC Alexander-Graham-Bell PhD scholarship. D.P.B. holds the GSK Chair in Diabetes of Université de Sherbrooke and a Fonds de Recherche du Québec - Santé (FRQS) J1 salary award. S.A.S. is a recipient of a CIHR Vanier PhD scholarship. A.C.C. holds the Canada Research Chair in Molecular Imaging of Diabetes.

AUTHOR CONTRIBUTIONS

Conceptualization, A.C.C., M.L., D.P.B., J.D.S., G.R.S., K.M.M., E.E.T, and B.G.; Methodology: A.C.C., M.L., D.P.B., G.R., J.D.S., G.R.S., K.M.M., M.G.S., J.D.S., E.E.T, M.F., S.P., F.F., S.D., and B.G.; Investigation: A.C.C., D.P.B., G.R., S.A.S., L.R., M.E.F., M.F., S.P., F.F., E.E.T., and B.G.; Writing – first draft: G.R., D.P.B., A.C.C., and S.A.S.; Writing – review & editing: S.A.S., G.R.S., K.M.M., M.G.S., J.D.S., A.C.C., B.G., M.L., S.D., and M.F.; Visualization: G.R. and S.A.S.; Funding Acquisition: A.C.C., J.D.S., G.R.S., and K.M.M.

DECLARATION OF INTERESTS

A.C.C. received research funding by Eli Lilly (2019–2021) and NovoNordisk (2021–ongoing) and consultation fees by HLS Therapeutics, Janssen Inc., Novartis Pharmaceuticals Canada Inc., and Novo Nordisk Canada Inc. K.M.M. is an advisory board member for NovoNordisk.

Received: January 14, 2022
Revised: June 14, 2022
Accepted: August 23, 2022
Published: September 20, 2022

REFERENCES

1. Zavaroni, I., Chen, Y.D., and Reaven, G.M. (1982). Studies of the mechanism of fructose-induced hypertriglyceridemia in the rat. Metabolism *31*, 1077–1083.
2. Nikkilä, E.A., and Ojala, K. (1965). Induction of hyperglyceridemia by fructose in the rat. Life Sci. *4*, 937–943.
3. Martinez, F.J., Rizza, R.A., and Romero, J.C. (1994). High-fructose feeding elicits insulin resistance, hyperinsulinism, and hypertension in normal mongrel dogs. Hypertension *23*, 456–463.
4. Hwang, I.S., Ho, H., Hoffman, B.B., and Reaven, G.M. (1987). Fructose-induced insulin resistance and hypertension in rats. Hypertension *10*, 512–516.
5. Stanhope, K.L., Schwarz, J.M., Keim, N.L., Griffen, S.C., Bremer, A.A., Graham, J.L., Hatcher, B., Cox, C.L., Dyachenko, A., Zhang, W., et al. (2009). Consuming fructose-sweetened, not glucose-sweetened, beverages increases visceral adiposity and lipids and decreases insulin sensitivity in overweight/obese humans. J. Clin. Invest. *119*, 1322–1334.
6. Stanhope, K.L., Bremer, A.A., Medici, V., Nakajima, K., Ito, Y., Nakano, T., Chen, G., Fong, T.H., Lee, V., Menorca, R.I., et al. (2011). Consumption of fructose and high fructose corn syrup increase postprandial triglycerides, LDL-cholesterol, and apolipoprotein-B in young men and women. J. Clin. Endocrinol. Metab. *96*, 1596–1605.
7. Stanhope, K.L., Medici, V., Bremer, A.A., Lee, V., Lam, H.D., Nunez, M.V., Chen, G.X., Keim, N.L., and Havel, P.J. (2015). A dose-response study of consuming high-fructose corn syrup-sweetened beverages on lipid/lipoprotein risk factors for cardiovascular disease in young adults. Am. J. Clin. Nutr. *101*, 1144–1154.
8. Hieronimus, B., Medici, V., Bremer, A.A., Lee, V., Nunez, M.V., Sigala, D.M., Keim, N.L., Havel, P.J., and Stanhope, K.L. (2020). Synergistic effects of fructose and glucose on lipoprotein risk factors for cardiovascular disease in young adults. Metabolism *112*, 154356.
9. Schwarz, J.M., Noworolski, S.M., Wen, M.J., Dyachenko, A., Prior, J.L., Weinberg, M.E., Herraiz, L.A., Tai, V.W., Bergeron, N., Bersot, T.P., et al. (2015). Effect of a high-fructose weight-maintaining diet on lipogenesis and liver fat. J. Clin. Endocrinol. Metab. *100*, 2434–2442.
10. Lustig, R.H., Mulligan, K., Noworolski, S.M., Tai, V.W., Wen, M.J., Erkin-Cakmak, A., Gugliucci, A., and Schwarz, J.M. (2016). Isocaloric fructose restriction and metabolic improvement in children with obesity and metabolic syndrome. Obesity *24*, 453–460.
11. Schwarz, J.M., Noworolski, S.M., Erkin-Cakmak, A., Korn, N.J., Wen, M.J., Tai, V.W., Jones, G.M., Palii, S.P., Velasco-Alin, M., Pan, K., et al. (2017). Effects of dietary fructose restriction on liver fat, de novo lipogenesis, and insulin kinetics in children with obesity. Gastroenterology *153*, 743–752.
12. Becher, T., Palanisamy, S., Kramer, D.J., Eljalby, M., Marx, S.J., Wibmer, A.G., Butler, S.D., Jiang, C.S., Vaughan, R., Schöder, H., et al. (2021). Brown adipose tissue is associated with cardiometabolic health. Nat. Med. *27*, 58–65.
13. Cypess, A.M., Lehman, S., Williams, G., Tal, I., Rodman, D., Goldfine, A.B., Kuo, F.C., Palmer, E.L., Tseng, Y.H., Doria, A., et al. (2009). Identification and importance of Brown adipose tissue in adult humans. N. Engl. J. Med. *360*, 1509–1517.
14. Ouellet, V., Routhier-Labadie, A., Bellemare, W., Lakhal-Chaieb, L., Turcotte, E., Carpentier, A.C., and Richard, D. (2011). Outdoor temperature, age, sex, body mass index, and diabetic status determine the prevalence, mass, and glucose-uptake activity of 18F-FDG-detected BAT in humans. J. Clin. Endocrinol. Metab. *96*, 192–199.
15. Wibmer, A.G., Becher, T., Eljalby, M., Crane, A., Andrieu, P.C., Jiang, C.S., Vaughan, R., Schöder, H., and Cohen, P. (2021). Brown adipose tissue is associated with healthier body fat distribution and metabolic benefits independent of regional adiposity. Cell Rep. Med. *2*, 100332.
16. Blondin, D.P., Labbé, S.M., Noll, C., Kunach, M., Phoenix, S., Guérin, B., Turcotte, É.E., Haman, F., Richard, D., and Carpentier, A.C. (2015). Selective impairment of glucose but not fatty acid or oxidative metabolism in brown adipose tissue of subjects with type 2 diabetes. Diabetes *64*, 2388–2397.
17. Orava, J., Nuutila, P., Noponen, T., Parkkola, R., Viljanen, T., Enerbäck, S., Rissanen, A., Pietiläinen, K.H., and Virtanen, K.A. (2013). Blunted metabolic responses to cold and insulin stimulation in brown adipose tissue of obese humans. Obesity *21*, 2279–2287.
18. Saari, T.J., Raiko, J., U-Din, M., Niemi, T., Taittonen, M., Laine, J., Savisto, N., Haaparanta-Solin, M., Nuutila, P., and Virtanen, K.A. (2020). Basal and cold-induced fatty acid uptake of human brown adipose tissue is impaired in obesity. Sci. Rep. *10*, 14373–14411.
19. Baskin, A.S., Linderman, J.D., Brychta, R.J., McGehee, S., Anflick-Chames, E., Cero, C., Johnson, J.W., O'Mara, A.E., Fletcher, L.A., Leitner, B.P., et al. (2018). Regulation of human adipose tissue activation, gallbladder size, and bile acid metabolism by A b3-adrenergic receptor agonist. Diabetes *67*, 2113–2125.
20. Blondin, D.P., Labbé, S.M., Tingelstad, H.C., Noll, C., Kunach, M., Phoenix, S., Guérin, B., Turcotte, E.E., Carpentier, A.C., Richard, D., and Haman, F. (2014). Increased brown adipose tissue oxidative capacity in cold-acclimated humans. J. Clin. Endocrinol. Metab. *99*, 438–446.
21. Blondin, D.P., Nielsen, S., Kuipers, E.N., Severinsen, M.C., Jensen, V.H., Miard, S., Jespersen, N.Z., Kooijman, S., Boon, M.R., Fortin, M., et al. (2020). Human Brown adipocyte thermogenesis is driven by β2-AR stimulation. Cell Metabol. *32*, 287–300.e7.
22. Cypess, A.M., Weiner, L.S., Roberts-Toler, C., Franquet Elía, E., Kessler, S.H., Kahn, P.A., English, J., Chatman, K., Trauger, S.A., Doria, A., and Kolodny, G.M. (2015). Activation of human brown adipose tissue by β3-adrenergic receptor agonist. Cell Metabol. *21*, 33–38.
23. Hanssen, M.J.W., Van Der Lans, A.A.J.J., Brans, B., Hoeks, J., Jardon, K.M.C., Schaart, G., Mottaghy, F.M., Schrauwen, P., and Van Marken Lichtenbelt, W.D. (2016). Short-term cold acclimation recruits brown adipose tissue in obese humans. Diabetes *65*, 1179–1189.
24. Hanssen, M.J.W., Hoeks, J., Brans, B., van der Lans, A.A.J.J., Schaart, G., van den Driessche, J.J., Jörgensen, J.A., Boekschoten, M.V., Hesselink, M.K.C., Havekes, B., et al. (2015). Short-term cold acclimation improves insulin sensitivity in patients with type 2 diabetes mellitus. Nat. Med. *21*, 863–865.
25. O'Mara, A.E., Johnson, J.W., Linderman, J.D., Brychta, R.J., McGehee, S., Fletcher, L.A., Fink, Y.A., Kapuria, D., Cassimatis, T.M., Kelsey, N., et al. (2020). Chronic mirabegron treatment increases human brown fat, HDL cholesterol, and insulin sensitivity. J. Clin. Invest. *130*, 2209–2219.
26. Zhao, S., Jang, C., Liu, J., Uehara, K., Gilbert, M., Izzo, L., Zeng, X., Trefely, S., Fernandez, S., Carrer, A., et al. (2020). Dietary fructose feeds hepatic lipogenesis via microbiota-derived acetate. Nature *579*, 586–591.
27. Sun, W., Dong, H., and Wolfrum, C. (2021). Local acetate inhibits brown adipose tissue function. Proc. Natl. Acad. Sci. USA *118*. e2116125118.
28. Li, J.M., Yu, R., Zhang, L.P., Wen, S.Y., Wang, S.J., Zhang, X.Y., Xu, Q., and Kong, L.D. (2019). Dietary fructose-induced gut dysbiosis promotes mouse hippocampal neuroinflammation: a benefit of short-chain fatty acids. Microbiome *7*, 98.

29. Blondin, D.P., Frisch, F., Phoenix, S., Guérin, B., Turcotte, É.E., Haman, F., Richard, D., and Carpentier, A.C. (2017). Inhibition of intracellular triglyceride lipolysis suppresses cold-induced brown adipose tissue metabolism and increases shivering in humans. Cell Metabol. *25*, 438–447.

30. David, L.A., Maurice, C.F., Carmody, R.N., Gootenberg, D.B., Button, J.E., Wolfe, B.E., Ling, A.V., Devlin, A.S., Varma, Y., Fischbach, M.A., et al. (2014). Diet rapidly and reproducibly alters the human gut microbiome. Nature *505*, 559–563.

31. Ouellet, V., Labbé, S.M., Blondin, D.P., Phoenix, S., Guérin, B., Haman, F., Turcotte, E.E., Richard, D., and Carpentier, A.C. (2012). Brown adipose tissue oxidative metabolism contributes to energy expenditure during acute cold exposure in humans. J. Clin. Invest. *122*, 545–552.

32. Richard, M.A., Blondin, D.P., Noll, C., Lebel, R., Lepage, M., and Carpentier, A.C. (2019). Determination of a pharmacokinetic model for [11C]-acetate in brown adipose tissue. EJNMMI Res. *9*, 31.

33. Richard, G., Noll, C., Archambault, M., Lebel, R., Tremblay, L., Ait-Mohand, S., Guérin, B., Blondin, D.P., Carpentier, A.C., and Lepage, M. (2021). Contribution of perfusion to the 11C-acetate signal in brown adipose tissue assessed by DCE-MRI and 68Ga-DOTA PET in a rat model. Magn. Reson. Med. *85*, 1625–1642.

34. Labbé, S.M., Croteau, E., Grenier-Larouche, T., Frisch, F., Ouellet, R., Langlois, R., Guérin, B., Turcotte, E.E., and Carpentier, A.C. (2011). Normal postprandial nonesterified fatty acid uptake in muscles despite increased circulating fatty acids in type 2 diabetes. Diabetes *60*, 408–415.

35. Oreskovich, S.M., Ong, F.J., Ahmed, B.A., Konyer, N.B., Blondin, D.P., Gunn, E., Singh, N.P., Noseworthy, M.D., Haman, F., Carpentier, A.C., et al. (2019). Magnetic resonance imaging reveals human brown adipose tissue is rapidly activated in response to cold. J. Endocr. Soc. *3*, 2374–2384.

36. Coolbaugh, C.L., Damon, B.M., Bush, E.C., Welch, E.B., and Towse, T.F. (2019). Cold exposure induces dynamic , heterogeneous alterations in human brown adipose tissue lipid content. Sci. Rep. *9*, 13600–13613. https://doi.org/10.1038/s41598-019-49936-x.

37. Abreu-Vieira, G., Sardjoe Mishre, A.S.D., Burakiewicz, J., Janssen, L.G.M., Nahon, K.J., van der Eijk, J.A., Riem, T.T., Boon, M.R., Dzyubachyk, O., Webb, A.G., et al. (2020). Human Brown adipose tissue estimated with magnetic resonance imaging undergoes changes in composition after cold exposure: an in vivo MRI study in healthy volunteers. Front. Endocrinol. *10*, 1–15.

38. Ahmed, B.A., Ong, F.J., Barra, N.G., Blondin, D.P., Gunn, E., Oreskovich, S.M., Szamosi, J.C., Syed, S.A., Hutchings, E.K., Konyer, N.B., et al. (2021). Lower brown adipose tissue activity is associated with non-alcoholic fatty liver disease but not changes in the gut microbiota. Cell Rep. Med. *2*, 100397.

39. Baba, S., Jacene, H.A., Engles, J.M., Honda, H., and Wahl, R.L. (2010). CT hounsfield units of Brown adipose tissue increase with activation: preclinical and clinical studies. J. Nucl. Med. *51*, 246–250.

40. Gifford, A., Towse, T.F., Walker, R.C., Avison, M.J., and Welch, E.B. (2016). Characterizing active and inactive brown adipose tissue in adult humans using PET-CT and MR imaging. Am. J. Physiol. Endocrinol. Metab. *311*, E95–E104.

41. Lundström, E., Strand, R., Johansson, L., Bergsten, P., Ahlström, H., and Kullberg, J. (2015). Magnetic resonance imaging cooling-reheating protocol indicates decreased fat fraction via lipid consumption in suspected brown adipose tissue. PLoS One *10*. e0126705–13.

42. Hamilton, G., Smith, D.L., Bydder, M., Nayak, K.S., and Hu, H.H. (2011). MR properties of brown and white adipose tissues. J. Magn. Reson. Imag. *34*, 468–473.

43. Patlak, C.S., and Blasberg, R.G. (1983). Graphical evaluation of blood-to-brain transfer constants from multiple-time uptake data. J. Cerebr. Blood Flow Metabol. *5*, 584–590.

44. Virtanen, K.A., Peltoniemi, P., Marjamäki, P., Asola, M., Strindberg, L., Parkkola, R., Huupponen, R., Knuuti, J., Lönnroth, P., and Nuutila, P. (2001). Human adipose tissue glucose uptake determined using [18F]-fluoro-deoxy-glucose ([18F]FDG) and PET in combination with microdialysis. Diabetologia *44*, 2171–2179.

45. Peltoniemi, P., Lönnroth, P., Laine, H., Oikonen, V., Tolvanen, T., Grönroos, T., Strindberg, L., Knuuti, J., and Nuutila, P. (2000). Lumped constant for [18F]fluorodeoxyglucose in skeletal muscles of obese and nonobese humans. Am. J. Physiol. Endocrinol. Metabol. *279*, 1122–1130.

46. Adiels, M., Olofsson, S.O., Taskinen, M.R., and Borén, J. (2008). Overproduction of very low-density lipoproteins is the hallmark of the dyslipidemia in the metabolic syndrome. Arterioscler. Thromb. Vasc. Biol. *28*, 1225–1236.

47. Serlie, M., and Serlie, M.J. (2017). Fructose consumption, lipogenesis, and non-alcoholic fatty liver disease. Nutrients *9*, 981–1020.

48. Alves-Bezerra, M., and Cohen, D.E. (2018). Triglyceride metabolism in the liver. Compr. Physiol. *8*, 1–22.

49. Blondin, D.P., Tingelstad, H.C., Noll, C., Frisch, F., Phoenix, S., Guérin, B., Turcotte, É.E., Richard, D., Haman, F., and Carpentier, A.C. (2017). Dietary fatty acid metabolism of brown adipose tissue in cold-acclimated men. Nat. Commun. *8*, 14146.

50. Hankir, M.K., Kranz, M., Keipert, S., Weiner, J., Andreasen, S.G., Kern, M., Patt, M., Klöting, N., Heiker, J.T., Brust, P., et al. (2017). Dissociation between brown adipose tissue 18F-FDG uptake and thermogenesis in uncoupling protein 1-deficient mice. J. Nucl. Med. *58*, 1100–1103.

51. Olsen, J.M., Csikasz, R.I., Dehvari, N., Lu, L., Sandström, A., Öberg, A.I., Nedergaard, J., Stone-Elander, S., and Bengtsson, T. (2017). β3-Adrenergically induced glucose uptake in brown adipose tissue is independent of UCP1 presence or activity: mediation through the mTOR pathway. Mol. Metabol. *6*, 611–619.

52. Richard, M.A., Pallubinsky, H., and Blondin, D.P. (2020). Functional characterization of human brown adipose tissue metabolism. Biochem. J. *477*, 1261–1286.

53. Low, W.S., Cornfield, T., Charlton, C.A., Tomlinson, J.W., and Hodson, L. (2018). Sex differences in hepatic De Novo lipogenesis with acute fructose feeding. Nutrients *10*.

54. Taskinen, M.R., Söderlund, S., Bogl, L.H., Hakkarainen, A., Matikainen, N., Pietiläinen, K.H., Räsänen, S., Lundbom, N., Björnson, E., Eliasson, B., et al. (2017). Adverse effects of fructose on cardiometabolic risk factors and hepatic lipid metabolism in subjects with abdominal obesity. J. Intern. Med. *282*, 187–201.

55. Worthmann, A., John, C., Rühlemann, M.C., Baguhl, M., Heinsen, F.A., Schaltenberg, N., Heine, M., Schlein, C., Evangelakos, I., Mineo, C., et al. (2017). Cold-induced conversion of cholesterol to bile acids in mice shapes the gut microbiome and promotes adaptive thermogenesis. Nat. Med. *23*, 839–849.

56. Scheja, L., and Heeren, J. (2016). Metabolic interplay between white, beige, brown adipocytes and the liver. J. Hepatol. *64*, 1176–1186.

57. Olsen, J.M., Sato, M., Dallner, O.S., Sandström, A.L., Pisani, D.F., Chambard, J.C., Amri, E.Z., Hutchinson, D.S., and Bengtsson, T. (2014). Glucose uptake in brown fat cells is dependent on mTOR complex 2-promoted GLUT1 translocation. J. Cell Biol. *207*, 365–374.

58. Herman, M.A., and Birnbaum, M.J. (2021). Molecular aspects of fructose metabolism and metabolic disease. Cell Metabol. *33*, 2329–2354.

59. Berbée, J.F.P., Boon, M.R., Khedoe, P.P.S.J., Bartelt, A., Schlein, C., Worthmann, A., Kooijman, S., Hoeke, G., Mol, I.M., John, C., et al. (2015). Brown fat activation reduces hypercholesterolaemia and protects from atherosclerosis development. Nat. Commun. *6*, 6356.

60. Khedoe, P.P.S.J., Hoeke, G., Kooijman, S., Dijk, W., Buijs, J.T., Kersten, S., Havekes, L.M., Hiemstra, P.S., Berbée, J.F.P., Boon, M.R., and Rensen, P.C.N. (2015). Brown adipose tissue takes up plasma triglycerides mostly after lipolysis. J. Lipid Res. *56*, 51–59.

61. Bartelt, A., Bruns, O.T., Reimer, R., Hohenberg, H., Ittrich, H., Peldschus, K., Kaul, M.G., Tromsdorf, U.I., Weller, H., Waurisch, C., et al. (2011).

Brown adipose tissue activity controls triglyceride clearance. Nat. Med. *17*, 200–205.

62. U Din, M., Saari, T., Raiko, J., Kudomi, N., Maurer, S.F., Lahesmaa, M., Fromme, T., Amri, E.Z., Klingenspor, M., Solin, O., et al. (2018). Postprandial oxidative metabolism of human Brown fat indicates thermogenesis. Cell Metabol. *28*, 207–216.e3.
63. U Din, M., Raiko, J., Saari, T., Kudomi, N., Tolvanen, T., Oikonen, V., Teuho, J., Sipilä, H.T., Savisto, N., Parkkola, R., et al. (2016). Human brown adipose tissue [15O]O2 PET imaging in the presence and absence of cold stimulus. Eur. J. Nucl. Med. Mol. Imag. *43*, 1878–1886.
64. Powell, E.S., Smith-Taillie, L.P., and Popkin, B.M. (2016). Added sugars intake across the distribution of US children and adult consumers: 1977-2012. J. Acad. Nutr. Diet. *116*, 1543–1550.e1.
65. Vos, M.B., Kimmons, J.E., Gillespie, C., Welsh, J., and Blanck, H.M. (2008). Dietary fructose consumption among US children and adults: the third national health and nutrition examination survey. Medscape J. Med. *10*, 160.
66. Haman, F., Péronnet, F., Kenny, G.P., Massicotte, D., Lavoie, C., Scott, C., and Weber, J.M. (2002). Effect of cold exposure on fuel utilization in humans: plasma glucose, muscle glycogen, and lipids. J. Appl. Physiol. *93*, 77–84.
67. Wolfe, R.R., and Chinkes, D.L. (2005). Isotope Tracers in Metabolic Research : Principles and Practice of Kinetic Analysis (Wiley-Liss).
68. Pouteau, E., Meirim, I., Métairon, S., and Fay, L.B. (2001). Acetate, propionate and butyrate in plasma: determination of the concentration and isotopic enrichment by gas chromatography/mass spectrometry with positive chemical ionization. J. Mass Spectrom. *36*, 798–805.
69. Tsukahara, T., Matsukawa, N., Tomonaga, S., Inoue, R., Ushida, K., and Ochiai, K. (2014). High-sensitivity detection of short-chain fatty acids in porcine ileal, cecal, portal and abdominal blood by gas chromatography-mass spectrometry. Anim. Sci. J. *85*, 494–498.
70. Stearns, J.C., Davidson, C.J., Mckeon, S., Whelan, F.J., Fontes, M.E., Schryvers, A.B., Bowdish, D.M.E., Kellner, J.D., and Surette, M.G. (2015). Culture and molecular-based profiles show shifts in bacterial communities of the upper respiratory tract that occur with age. ISME J. *9*, 1268.
71. Szamosi, J.C., Forbes, J.D., Copeland, J.K., Knox, N.C., Shekarriz, S., Rossi, L., Graham, M., Bonner, C., Guttman, D.S., Van Domselaar, G., et al. (2020). Assessment of inter-laboratory variation in the characterization and analysis of the mucosal microbiota in Crohn's disease and ulcerative colitis. Front. Microbiol. *11*, 1–13.
72. Bartram, A.K., Lynch, M.D.J., Stearns, J.C., Moreno-Hagelsieb, G., and Neufeld, J.D. (2011). Generation of multimillion-sequence 16S rRNA gene libraries from complex microbial communities by assembling paired-end Illumina reads. Appl. Environ. Microbiol. *77*, 3846–3852.
73. Callahan, B.J., McMurdie, P.J., Rosen, M.J., Han, A.W., Johnson, A.J.A., and Holmes, S.P. (2016). DADA2: high-resolution sample inference from Illumina amplicon data. Nat. Methods *13*, 581–583.
74. Martin, M. (2011). Cutadapt removes adapter sequences from high-throughput sequencing reads. EMBnet. J. *17*, 10.
75. Hardy, J.D., Du Bois, E.F., and Soderstrom, G.F. (1938). The technic of measuring radiation and convection. J. Nutr. *15*, 461–475. https://doi.org/10.1093/jn/15.5.461.
76. Haman, F., Legault, S.R., Rakobowchuk, M., Ducharme, M.B., and Weber, J.M. (2004). Effects of carbohydrate availability on sustained shivering II. Relating muscle recruitment to fuel selection. J. Appl. Physiol. *96*, 41–49.
77. Haman, F., Péronnet, F., Kenny, G.P., Massicotte, D., Lavoie, C., and Weber, J.M. (2005). Partitioning oxidative fuels during cold exposure in humans: muscle glycogen becomes dominant as shivering intensifies. J. Physiol. *566*, 247–256.
78. Blondin, D.P., Labbé, S.M., Phoenix, S., Guérin, B., Turcotte, É.E., Richard, D., Carpentier, A.C., and Haman, F. (2015). Contributions of white and brown adipose tissues and skeletal muscles to acute cold-induced metabolic responses in healthy men. J. Physiol. *593*, 701–714.
79. Bell, D.G., Tikuisis, P., and Jacobs, I. (1992). Relative intensity of muscular contraction during shivering. J. Appl. Physiol. *72*, 2336–2342. https://doi.org/10.1152/jappl.1992.72.6.2336.
80. Haman, F., Legault, S.R., and Weber, J.M. (2004). Fuel selection during intense shivering in humans: EMG pattern reflects carbohydrate oxidation. J. Physiol. *556*, 305–313.
81. Vella, A., and Rizza, R.A. (2009). Application of isotopic techniques using constant specific activity or enrichment to the study of carbohydrate metabolism. Diabetes *58*, 2168–2174.
82. Buck, A., Wolpers, H.G., Hutchins, G.D., Savas, V., Mangner, T.J., Nguyen, N., and Schwaiger, M. (1991). Effect of carbon-11-acetate recirculation on estimates of myocardial oxygen consumption by PET. J. Nucl. Med. *32*, 1950–1957.
83. Vanhamme, L., van den Boogaart, A., and Van Huffel, S. (1997). Improved method for accurate and efficient quantification of MRS data with use of prior knowledge. J. Magn. Reson. *129*, 35–43.
84. Peterson, P., Trinh, L., and Månsson, S. (2021). Quantitative 1H MRI and MRS of fatty acid composition. Magn. Reson. Med. *85*, 49–67.
85. Patterson, B.W., Zhao, G., Elias, N., Hachey, D.L., and Klein, S. (1999). Validation of a new procedure to determine plasma fatty acid concentration and isotopic enrichment. J. Lipid Res. *40*, 2118–2124.

STAR★METHODS

KEY RESOURCES TABLE

REAGENT or RESOURCE	SOURCE	IDENTIFIER
Biological samples		
Human plasma samples	This paper	N/A
Human stool samples	This paper	N/A
Human urine sample	This paper	N/A
Human plasma control	BioIVT	#HMPLEDTA2
Chemicals, peptides, and recombinant proteins		
Zinc Sulfate Solution	Z2876	Sigma Aldrich
Barium Sulfate Solution	B4059	Sigma Aldrich
Auto kit Glucose	Wako Diagnostics U.S.A. Corporation	997-03001
NEFA	Wako Diagnostics U.S.A. Corporation	995-34791 999-34691 993-35191 991-34891
Triglyceride	Wako Diagnostics U.S.A. Corporation	461-08992 461-09092
C-peptide, GIP, GLP-1 total, Glucagon, Insulin, Leptin, PYY	Millipore-Sigma	HMH3-34K-07
Human Ghrelin total	Millipore-Sigma	EZGRT-89K
Acylated ghrelin human ELISA	bertin pharma	A05106-96
HMW Total adiponectin	ALPCO	80-ADPHU-E01
Taq DNA Polymerase, Recombinant	Life Technologies	10342020
Critical commercial assays		
MagMAX™-96 DNA Multi-Sample Kit	Invitrogen	4413021
SequalPrep normalization kit	ThermoFisher	A1051001
Deposited data		
Raw and analyzed data	This paper	Zenodo: https://doi.org/10.5281/zenodo.5834789
Pharmacokinetic modeling tool for MATLAB	This paper	Zenodo: https://doi.org/10.5281/zenodo.5834789
16S rRNA v34 Sequencing Data	This paper	BioProject ID: PRJNA793467 (www.ncbi.nlm.nih.gov/bioproject/PRJNA793467)
Oligonucleotides		
dNTPs Solution, Mix	New England Biolabs	N0447L
341F (CCTACGGGNGGCWGCAG)	Bartram et al. (https://doi.org/10.1128/AEM.02772-10)	
806R (GGACTACNVGGGTWTCTAAT)	Bartram et al. (https://doi.org/10.1128/AEM.02772-10)	
Software and algorithms		
GraphPad Prism 9 for statistical analysis	GraphPad Software	RRID: SCR_002798
MassLynx V.4.1	Waters	SCN714
PMOD 3.7	PMOD Technologies LLC	RRID: SCR_016547
Adobe Photoshop	Adobe	RRID: SCR_014199
GNU Image Manipulation Program 2.10	www.gimp.org	RRID: SCR_003182
MATLAB R2019a	The MathWorks	RRID: SCR_001622
DADA2 Version 1.14	Callahan et al. (https://doi.org/10.1038/nmeth.3869)	

(*Continued on next page*)

Continued

REAGENT or RESOURCE	SOURCE	IDENTIFIER
Cutadapt Version 1.18	Marcel Martin (https://doi.org/10.14806/ej.17.1.200)	RRID: SCR_011841
SILVA database Version 1.3.8	Quast et al. (https://doi.org/10.1093/nar/gks1219) Yilmaz et al. (https://doi.org/10.1093/nar/gkt1209)	RRID: SCR_006423
microViz Version 0.7.3	Barnett et al. (https://doi.org/10.5281/zenodo.4644057)	
tidyverse Version 1.3.1	Wickham et al. (https://doi.org/10.21105/joss.01686)	RRID: SCR_019186
phyloseq Version 1.32.0	McMurdie and Holmes (https://doi.org/10.1371/journal.pone.0061217)	RRID: SCR_013080
vegan Version 2.5–7	Oksanen et al. (URL: https://cran.r-project.org/web/packages/vegan/index.html)	RRID: SCR_011950
ggplot2 Version 3.3.3	Wickham (URL: https://ggplot2.tidyverse.org)	RRID: SCR_014601
ggpubr Version 0.4.0	Kassambara (URL: https://cran.r-project.org/web/packages/ggpubr/index.html)	RRID: SCR_021139
viridis Version 0.6.0	Garnier et al. (https://doi.org/10.5281/zenodo.4679424)	RRID: SCR_016696
lme4 Version 1.1–27	Bates et al. (https://doi.org/10.18637/jss.v067.i01)	RRID: SCR_015654
emmeans Version 1.6.1	Lenth (URL: https://CRAN.R-project.org/package=emmeans)	RRID: SCR_018734
RStudio Version 1.2.5042	RStudio Team (URL: http://www.rstudio.com/)	RRID: SCR_000432
R Version 4.0.0	R Core Team (URL: https://www.R-project.org)	RRID: SCR_001905
Other		
[^{11}C]acetate, radiotracer	CIMS	N/A
[^{18}F]FDG, radiotracer	CIMS	N/A
[3-^{3}H]glucose, stable isotope tracer	PerkinElmer	Cat# NET331A005MC
[1,1,2,3,3-^{2}H]glycerol, stable isotope tracer	Cambridge Isotopes	Cat# DLM-1229
[U-^{13}C]palmitate, stable isotope tracer	Cambridge Isotopes	Cat# CLM-3934
MTBSTFA + 1% t-BDMSC	Millipore-Sigma	M-108
^{13}C- glycerol	Cambridge Isotope Laboratories	CLM-1397
U^{13}C-Linoleic Acid potassium salt	Cambridge Isotope Laboratories	CLM-8835
Palmitic Acid	Millipore-Sigma	P5585
Oleic Acid	Millipore-Sigma	O1008
Linoleic Acid	Millipore-Sigma	L1376
Sodium butyrate	Millipore-Sigma	B5887
Sodium propionate	Millipore-Sigma	P1880
Sodium acetate	Millipore-Sigma	S2889
GC-MSMS	Waters	Quattro Micro-GC
Gemini TF PET-CT scanner	Philips	N/A
Ingenia 3.0T MR system	Philips	N/A
Liquid-conditioned suit	Med-Eng	Cat# 1004340
Isotemp 6200R28 water bath	Fisher Scientific	Cat# 13-874-676
Vmax 29n (indirect calorimetry)	SensorMedics	N/A
Thermochron iButton	Maxim	Cat # DS1922H
Myomonitor IV EMG system	Delsys	N/A
Horizon QDR DXA	Hologic	N/A
Beta Counter LS 6500	Beckman Coulter	N/A
Optima L-100XP ultracentrifuge	Beckman Coulter	N/A
MagMAX Express 96-Deep Well Magnetic Particle Processor	Applied Biosystems	N/A
MiSeq System	Illumina	N/A

RESOURCE AVAILABILITY

Lead contact

Further information and requests for resources and reagents should be directed to and will be fulfilled by the lead contact, André Carpentier (andre.carpentier@usherbrooke.ca).

Materials availability

This study did not generate unique reagents.

Data and code availability

- The processed data generated during this study as well as the MATLAB code used to perform the pharmacokinetic modeling of ^{18}F-FDG and ^{11}C-acetate are available at Zenodo: https://doi.org/10.5281/zenodo.5834789.
- The 16S rRNA v34 sequencing data from the microbiome analysis is available at BioProject ID: PRJNA793467 (www.ncbi.nlm.nih.gov/bioproject/PRJNA793467).
- Anonymized image files are voluminous, and therefore, not deposited in any public repository, but can be made available on request to the lead contact (andre.carpentier@usherbrooke.ca).

EXPERIMENTAL MODEL AND SUBJECT DETAILS

Human subjects

The protocol received approval from the Human Ethics Committee of the Centre de Recherche du Centre hospitalier universitaire de Sherbrooke. Written informed consent was obtained from all participants in accordance with the Declaration of Helsinki. The study was prospectively registered on ClinicalTrials.gov (NCT03188835) on June 13, 2017. A total of 16 male participants were recruited for this study (Figure S1) with the first participant enrolling on July 6, 2017. However, 5 withdrew before undertaking any experimental procedures. Of the remaining 11 participants, 1 withdrew following the baseline imaging protocol and 1 was excluded from analyses of carbohydrate-enriched diets (but not baseline) due to antibiotic use potentially affecting the microbiome. Metabolic data for this last participant were still analyzed and shown on graphs using a different symbol shape. Characteristics of participants can be found in Table S1. The inclusion criteria were as follows: (i) male; (ii) age between 20 and 40 years-old; (iii) BMI <30 kg/m^2; (iv) normal glucose tolerance (blood glucose <7.8 mmol/L 2 h post 75 g oral glucose tolerance test); (v) no first-degree familial history of type 2 diabetes (parent or sibling). Exclusion criteria comprised: (i) fasting plasma triglycerides >5.0 mmol/L or history of total cholesterol >7 mmol/L; (ii) consuming more than 2 alcoholic beverages per day; (iii) smoking more than 1 cigarette per day; (iv) history of total cholesterol level >7 mmol/L, of cardiovascular disease or hypertensive crisis; (v) treatment with fibrates, thiazolidinedione, insulin, beta-blocker or other drugs with effects on insulin resistance or lipid metabolism (exception for anti-hypertensive drugs, statins or metformin); (vi) presence of a non-controlled thyroid disease, renal or hepatic disease, history of pancreatitis, bleeding disorder, cardiovascular disease or any other serious medical condition; (vii) history of serious gastrointestinal disorders (malabsorption, peptic ulcer, gastro-esophageal reflux having required a surgery, etc.); (viii) contraindication to MR imaging (e.g., metal implant) or PET/CT imaging (e.g., having undergone a scan in the last 12 months); (ix) chronic administration of any other medication.

METHOD DETAILS

Study design

Figure S2 summarizes the study protocols. Briefly, participants were asked to follow three 14-day dietary protocols. The first protocol (A) consisted of a balanced diet for baseline measures. The other two protocols consisted of the same baseline diet supplemented with a high fructose (B) or glucose (C) drink, each representing 25% of energy intake. Protocols B and C were randomized and separated by a 1-month washout period during which participants followed the baseline diet. After each diet protocol, participants provided stool samples for microbiome analysis and underwent a metabolic study day with cold exposure to stimulate BAT thermogenesis. During the metabolic study days, body composition was assessed by dual-energy X-ray absorptiometry (DXA) and magnetic resonance (MR). Whole-body energy expenditure and substrate metabolism were measured by indirect calorimetry and stable isotope tracers. Tissue-specific glucose uptake was assessed by ^{18}F-FDG PET, and oxidative metabolism was assessed by ^{11}C-acetate PET. Participants were fasted for 12 h and abstained from strenuous physical activity for 48 h prior to metabolic study days.

Measures of body composition and energy expenditure

Body composition was assessed by DXA (Hologic) and bioelectrical impedance (Tanita). Whole-body energy expenditure at rest was determined by indirect respiratory calorimetry with correction for protein oxidation[66] for a duration of 20 min per measure. These measures were taken on visits 2, 3, 4, 5 and 6. On imaging visits (visits 3, 4 and 6), the indirect calorimetry (SensorMedics Vmax) was performed once at room temperature (before cooling) and twice during cold exposure (the reported cold exposure data is the average of both measures). The molar rate of fatty acid oxidation was determined by converting the rate of triglyceride oxidation

(mg/min) to its molar equivalent (μmol/min), assuming the average molecular weight of human triglyceride is 860 g/mol and multiplying the molar rate of triglyceride oxidation by three, as each mole of triglyceride contains three moles of fatty acids.[67] Energy potentials of 16.3, 40.8 and 19.7 kJ/g were used to calculate the amount of heat produced from glucose, lipid, and protein oxidation, respectively, and converted to a rate in $kJ \cdot min^{-1}$. The level of physical activity of each participant was assessed with a uniaxial accelerometer (Caltrac) on 3 consecutive days during each diet protocol (before visits 3, 4 and 6).

Diets

The baseline, isocaloric, meal plans were designed by a registered dietician (S.D.) following the recommendations of the 2007 Canada's Food Guide (~50% carbohydrates, ~30% lipids and ~20% proteins) as well as the dietary preferences and restrictions of each participant. Daily caloric needs were estimated based on resting metabolism (indirect calorimetry) and physical activity (uniaxial accelerometer). Alcohol and dietary supplements likely to affect the gastrointestinal microbiome were prohibited. Participants were asked to refrain from changing their dietary or exercise habits during the study. However, they were not asked to fill out food diaries or otherwise supervised to ensure compliance.

The fructose (protocol B) or glucose (protocol C) supplements were provided in powder form (Sigma-Aldrich) that participants dissolved in 1–1.5 L of water and drank throughout the day. Addition of pure lemon or orange juice (no artificial sweeteners) was suggested to make the drink more palatable. To improve tolerance, the amount of glucose or fructose consumed was gradually increased during the first 3 days of the study (15%, 20 and 25% of estimated daily energy requirements) and remained stable for the remaining 11 days (174 ± 37 g/day, equivalent to 655 ± 138 kcal/day).

Finally, participants fasted (water allowed) from 20 h 00 on the evening before the metabolic study until the end of procedures at approximately 16 h 30 the following day.

Stool sample collection and analysis

Stool samples were provided by participants after each diet protocol. Samples were kept frozen at −80°C until processed. Before analysis, samples were thawed either at 4°C (faecal short-chain fatty acid content) or room temperature (microbiome composition), and remaining portions were refrozen. Stool samples underwent analysis for SCFA (acetate, propionate, and butyrate) at Université de Sherbrooke, as well as microbiome composition at McMaster University.

Faecal SCFA content was measured by gas chromatography-tandem mass spectrometry (GC-MS/MS, Agilent GC model 7890A and Waters Quattro Micro) based on methods developed for blood samples.[68,69] The column was an Agilent DB-5ms Ultra Inert (30 m, 0.25 mm, 0.25 μm) with helium as the carrier gas. Each sample was analyzed in triplicate. All samples from a same participant were analyzed at the same time to limit variability. Approximately 150 mg of sample was transferred to a 2 mL polypropylene microtube with glass beads and weighted to obtain wet weight. Then, 1 mL of 0.2% HCL was added, and the sample was shaken on ice for 20 min before centrifugation (9400 g, 5 min). The supernatant was transferred to a 2 mL polypropylene tube and recentrifuged (9400 g, 2 min). The pellet was conserved for estimation of dry weight. For sample analysis, 20 μL of diluted internal standard (acetate-d_3 25 mM, propionate-d_5 5 mM or butyrate-d_5 5 mM) was added to a 2 mL crimp top vial, followed by 250 μL of 0.4% HCL, 180 μL of deionised water, 50 μL of the supernatant, and 1 mL of dichloromethane. The tube was closed with the crimp cap and mixed with a shaker (10 min, room temperature) before being centrifuged upside down (800 g, 5 min). Approximately 600 μL of the dichloromethane phase was drawn from the upside-down vial with a glass syringe (avoiding any water). The dichloromethane solution was transferred to a 2 mL glass vial containing 400 mg of dry sodium sulfate. The glass vial was closed and allowed to sit for 1 h at room temperature. Finally, 20 μL of the derivatization reagent (MTBSTFA +1% t-BDMCS reagent diluted 1:100 in dichloromethane) was added to a 2 mL screw-tread vial with a 200 μL, 6 × 29 mm glass insert (mandrel precision point, 33 glass, with plastic spring; Chromatographic Specialties), followed by 200 μL of sample extract (dichloromethane phase). The sample was then injected (3 μL) in the GC-MS/MS in split mode and using positive electron impact ionization for mass detection.

Genomic DNA was extracted as described previously[70] with some modifications.[71] Samples were transferred to screw cap tubes containing 2.8 mm ceramic beads, 0.1 mm glass beads, GES and sodium phosphate buffer. Samples were bead beat and centrifuged as described, and the supernatant was further processed using the MagMAX Express 96-Deep Well Magnetic Particle Processor from Applied Biosystems with the multi-sample kit (Life Technologies #4413022).

Purified DNA was used to amplify the v34 region of the 16S rRNA gene by PCR. 50 ng of DNA was used as template with 1U of Taq Polymerase, 1× Taq buffer, 1.5 mM MgCl2, 0.4 mg/mL BSA, 0.2 mM dNTPs, and 5 pmol each of 341F (CCTACGGGNGGCWGCAG) and 806R (GGACTACNVGGGTWTCTAAT) Illumina adapted primers, as described by Bartram et al.[72] The reaction was carried out at 94°C for 5 min, 5 cycles of 94°C for 30 s, 47°C for 30 s, and 72°C for 40 s, followed by 25 cycles of 94°C for 30 s, 50°C for 30 s and 72°C for 40 s, with a final extension of 72°C for 10 min. Resulting PCR products were visualized on a 1.5% agarose gel. Positive amplicons were normalized using the SequalPrep normalization kit (ThermoFisher #A1051001) and sequenced on the Illumina MiSeq platform at the McMaster genomics facility.

Reads were processed using DADA2.[73] First, Cutadapt was used to filter and trim adapter sequences and PCR primers from the raw reads with a minimum quality score of 30 and a minimum read length of 100 bp.[74] Sequence variants were then resolved from the trimmed raw reads using DADA2, an accurate sample inference pipeline from 16S amplicon data. DNA sequence reads were filtered and trimmed based on the quality of the reads for each Illumina run separately, error rates were learned, and sequence variants were

determined by DADA2. Sequence variant tables were merged to combine all information from separate Illumina runs. Bimeras were removed and taxonomy was assigned using the SILVA database version 1.3.8.

We filtered to all ASVs assigned to the kingdom bacteria and removed all ASVs assigned to the kingdom eukaryota, the order chloroplast and the family mitochondria. After filtering, 1,720,471 total reads (average: 61,445; range: 11,449–124,952) with 2517 total ASVs (average 199 ASVs/sample; range: 61–341) remained.

Please refer to the Quantification and statistical analysis section for details on the analysis methods.

BAT stimulation by cold exposure

On metabolic study days, subjects underwent a 3-h cooling protocol.[29] After the morning MRI session, subjects, wearing only shorts, were instrumented with autonomous wireless temperature sensors (Thermochron iButton model DS1922H, Maxim) placed on 12 sites to measure mean skin temperature[75]: forehead, upper back, lower back, abdomen, forearm, quadricep, hamstring, gastrocnemius, anterior tibialis, chest, bicep, and hand. Surface electromyography electrodes (Delsys, EMG System) were placed on the belly of eight muscles known to contribute significantly to shivering during cold exposure[76–79]: *m.* trapezius superior, *m.* sternocleidomastoid, *m.* pectoralis major, *m.* deltoideus, *m.* biceps brachii, *m.* rectus abdominis, *m.* vastus lateralis, *m* rectus femoris, and *m.* vastus medialis. To normalize the shivering measures, subjects performed a series of isometric maximal voluntary contractions for each muscle. Finally, participants were asked to put on a liquid conditioned suit (Three Piece, Med-Eng).

Cooling was started ~12 h 00 and maintained for 180 min. During this period, water at 18°C was perfused through tubing in the suit with a temperature- and flow-controlled circulation bath (Isotemp 6200R28, Fisher Scientific). Shivering and skin temperature were monitored continuously throughout the experiment. Shivering intensity and shivering pattern were determined as previously described.[76–78,80] Mean skin temperature was calculated using an area-weighted mean from the wireless temperature sensors.

Energy substrate turnover

On metabolic study days, after the morning MRI, participants were asked to empty their bladders and indwelling catheters (18G) were placed in the antecubital vein of both arms for blood sampling (right arm) and tracer infusion (left arm). A primed (3.3×10^6 dpm) continuous infusion (0.56×10^6 dpm min^{-1}) of [3-^{3}H]-glucose was initiated 150 min before the start of cold exposure to determine the plasma glucose appearance rate ($Ra_{glucose}$).[31,81] A bolus of [1-^{13}C]-$NaHCO_3$ (1.2 μmol kg^{-1}), followed by continuous infusion of [U-^{13}C]-palmitate (0.01 μmol $kg^{-1} \cdot min^{-1}$ in 100 mL 25% human serum albumin), and a primed (1.6 μmol kg^{-1}) continuous infusion (0.1 μmol $kg^{-1} \cdot min^{-1}$) of [1,1,2,3,3-^{2}H]-glycerol were started 60 min before the start of cold exposure to determine plasma NEFA appearance rate (Ra_{NEFA}) and plasma glycerol appearance rate ($Ra_{glycerol}$).

Ra_{NEFA} was calculated by multiplying the plasma palmitate appearance rate by the fractional contribution of palmitate to total plasma NEFA concentrations. Blood samples were collected for dosing of tracer enrichment and other metabolites before starting the infusion, before cooling, and every hour thereafter. Samples of expired air were also taken every hour to measure the enrichment in $^{13}CO_2$. Urine was collected at the end of the baseline period, 75 min into cold exposure and at the end of cold exposure to measure urea production. Rates of appearance for glucose, non-esterified fatty acids, and glycerol were reported for room temperature (t = 0, just before cold exposure) and the steady state of the cooling period (t = 120 and 180 min).

Imaging of triglyceride content by magnetic resonance imaging

On metabolic study days, MRI and MRS were performed in the morning (before cooling, at approximately 7:30) and evening (after cooling, at approximately 16:00) on a 3T Philips Ingenia scanner (Philips Healthcare). On both occasions, triglyceride content was assessed in the supraclavicular region and in the abdominal region.

Participants, wearing only the standard hospital gown, were placed on a dedicated table (Philips Healthcare) compatible with the MR and PET scanners. They were immobilized with a vacuum cushion (Vac-Lok; Civco Radiotherapy) to ensure consistent positioning throughout the day. In the morning, participants were wrapped in a warm blanket to ensure participants were not cold.

Images were acquired with an 8-channel torso surface coil (dStream; Philips) covering the neck, torso, and abdomen. Tables S2 and S3 summarize the MRI and MRS sequence parameters. Briefly, an anatomical T1-weighted image of the supraclavicular region was taken to localize BAT. Three 8 mm^3 voxels were placed in the supraclavicular fat for BAT proton spectroscopy. Voxel placement aimed at avoiding blood vessels and surrounding muscles while covering the largest volume possible (Figure S3). Since supraclavicular fat depots are bilateral, at least one voxel was placed on each side. To quantify fat content, mDixon Quant images were acquired covering the neck and shoulders. Similar sequences were performed for the liver region, except that a single 25 mm^3 voxel was placed in the right lobe of the liver, and a single 10 mm^3 voxel was placed in the subcutaneous fat of the lower back. Liver spectroscopy, Dixon imaging, and T1-weighted image of the liver were performed in breath hold (inspiration), other sequences were performed with free breathing.

Imaging of glucose metabolism and oxidative metabolism by PET/CT

A dynamic ^{11}C-acetate PET scan (Philips Gemini TF) was performed at room temperature at approximately 11:30 only for protocol A (baseline). For all protocols, a dynamic ^{11}C-acetate scan was performed at approximately 13:30 after 90 min of cooling. Each scan started with the injection of ^{11}C-acetate (~185 MBq, over 20 s with a 20 s saline flush) and was performed as a 30-min list-mode acquisition. A dynamic ^{18}F-FDG scan was performed at approximately 14:00 with a 2-min background, injection of the radiotracer

(~125 MBq, over 20 s with a 20 s normal saline flush) and 30-min list-mode acquisition. Finally, a whole-body (head to knee) static PET scan was performed at approximately 15:00, after the 3-h cooling period. This static scan measured ^{18}F-FDG distribution in different tissues without additional radiotracer injection.

Low-dose CT scans were obtained for anatomical reference and attenuation correction. A CT of the cervicothoracic region (120 kVp, 49 mA, 30 mAs) was done before each dynamic ^{11}C-acetate scan, and a whole-body CT (120 kVp, 30 mA, 16 mAs) was done before the whole-body ^{18}F-FDG scan. CT acquisition was not needed for the dynamic ^{18}F-FDG scan because the participant was in the same position as for the previous ^{11}C-acetate scan.

Image processing

MR images (Figure S3) were reconstructed online. Dynamic PET images (Figure S4) were reconstructed with a 3D RAMLA algorithm. Time frames for ^{11}C-acetate were: 24 × 10 s, 12 × 30 s, and 4 × 300 s. Time frames for ^{18}F-FDG were: 1 × 2 min (background), 12 × 10 s, 10 × 45 s, 7 × 90 s, and 2 × 300 s. The static ^{18}F-FDG image was reconstructed with a BLOB-OS-TF algorithm. CT reconstruction was performed with filtered back projection. Standard corrections for decay, attenuation (CT-based), scattering (single scatter simulation) and random coincidences (delayed window) were performed for PET. PET data was expressed in units of standardized uptake value ($SUV = \frac{Activity}{Injected\ \ dose} \cdot body\ weight$).

Regions of interest were segmented manually in PMOD (v. 3.7, Bruker). Axial CT images were used as anatomical references for PET segmentation. Axial T1-weighted images were used as anatomical reference for MRI segmentation. PET and MR images were also registered and segmented together, but this method proved less reliable due to small registration errors, and results were not presented in this article. The BAT region included all fat visible in the neck and supraclavicular fossa on both sides. Other BAT depots (e.g., paraspinal) were not segmented because they are not visible for all participants. Other segmented tissues include muscles (*m.* sternocleidomastoideus, *m.* trapezius, *m.* deltoideus, and *m.* pectoralis major), subcutaneous white adipose tissue (lower back for MRI and cervical for PET), abdominal visceral adipose tissue (excluding perirenal adipose tissue), and liver. For pharmacokinetic modeling, the arterial input function was extracted from a spherical region (diameter: 10 mm) in the aortic arch.

For static images, such as proton-density fat fraction maps from Dixon MRI, CT radiodensities, and static ^{18}F-FDG PET, average values were calculated for each region of interest. For dynamic PET imaging, time-activity curves were extracted for each region of interest. The blood signal for ^{11}C-acetate was then corrected to exclude the contribution of metabolites.[82]

Pharmacokinetic modeling was performed in MATLAB (The MathWorks, R2019a). A four-compartment, two-tissue, model[32] was applied to the ^{11}C-acetate signal to derive the rates of uptake (K_1 [ml·g^{-1}·min^{-1}]), oxidation (k_2 [min^{-1}]) and lipid synthesis (k_3 [min^{-1}]). For ^{11}C-acetate under cold condition, the blood volume fraction was constrained based on data from the ^{18}F-FDG three-compartment model.[33] Fractional glucose uptake (Ki [min^{-1}]) was also obtained from Patlak graphical analysis[43] and converted to metabolic rate of glucose using the plasma glucose level (MRGlu = K_i·glycemia·LC^{-1}·100 [μmol·100 g^{-1} min^{-1}]). This conversion assumes a lump constant (LC) value for ^{18}F-FDG compared with endogenous plasma glucose which was set at 1.14 for fat and 1.16 for muscles.[44,45]

Finally, MR spectra were processed in jMRUI and quantified with AMARES.[83] For BAT and scWAT, 6 gaussian peaks were considered: 0.9 ppm methyl, 1.3 ppm methylene/β-carboxyl, 2.1 ppm α-olefin/α-carboxyl, 4.2 ppm glycerol, 4.7 ppm water, and 5.3 ppm olefin/glycerol. For the liver, only the water and methylene peaks were visible. Correction for T1 and T2 decay was performed for each resonance. For T1, data from the literature was used.[42,84] For T2, correction was based on the multi-echo data for the liver and on the literature for BAT and scWAT.[42,84] Voxels with poor shimming or excessive signal contamination by other tissues were rejected. Values obtained for the different BAT voxels in a same participant and condition were averaged. The number of double bonds and methylene-interrupted double bonds were calculated for BAT and scWAT based on the method by Hamilton et al.[42]

Biological assays

Individual plasma NEFA (palmitate, linoleate, oleate) [U-^{13}C]-palmitate enrichment and [1,1,2,3,3-^{2}H]-glycerol enrichment were measured by GC-MS/MS (Agilent GC model 7890A and Waters Quattro Micro). The column was an Agilent DB-5ms Ultra Inert (30 m, 0.25 mm, 0.25 μm) with helium as the carrier gas. The precipitation method was based on that of Patterson et al[85] with some modifications. An aliquot of plasma (40 μL) was mixed with internal standard of $^{13}C_{18}$-linoeate (20 μL of 50 μM in acetone) and ^{13}C-glycerol (20 μL of 500 μM in water). Then, acetone (500 μL) was added, and the mixture was cooled at −20°C to allow protein precipitation. After centrifugation, (3500 g, 10 min), the supernatant was extracted, then mixed with deionised water (500 μL) and hexane (500 μL). After another centrifugation (3500 g, 10 min), the two phases were separated, and dried under vacuum. The organic phase residue, which contains free fatty acids was derivatized with a solution of MTBSTFA +1% t-BDMCS (8.2 mg, 34 μmol) and imidazole (54 ng, 0.8 nmol) in DMF. Aqueous phase residue for glycerol quantification was derivatized with a solution of MTBSTFA +1% t-BDMCS (20.7 mg, 86 μmol) and imidazole (136 ng, 2 nmol) in DMF (40 μL). After incubation (80°C, 1 h), samples were cooled down and then injected (1 μL) in the GC-MS/MS in split mode and using positive electron impact ionization for mass detection.

Tritium from [1-^{3}H]-glucose enrichment was detected by liquid scintillation spectrometry (Beckman Coulter LS 6500).

Plasma glucose, total NEFA triglycerides, cortisol, TSH, free T3 and free T4 were measured using specific radioimmunoassays and colorimetric assays. Plasma C-peptide, GIP, total GLP-1, glucagon, insulin, and leptin were measured using Luminex xMAP-based immunoassays (Millipore).

QUANTIFICATION AND STATISTICAL ANALYSIS

Sample size calculation

The sample size was based on a decrease of 50% in BAT oxidative metabolism from previously observed values (K_{mono} = 1.8 ± 0.5 min^{-1}). For a paired *t*-test with an α of 0.05 and a power of 80%, the required sample size was 9. This level of oxidative metabolism suppression seemed realistic based on previous data from pharmacological inhibition of BAT activity.[29] We planned to recruit 15 participants to account for potential incomplete data sets or losses to follow-up.

Statistical analysis

All microbiome analyses were conducted in RStudio (version 1.2.5042; April 2020) with R (version 4.0.0; April 2020) using the microViz, tidyverse, phyloseq, vegan, lme4, and emmeans packages for analysis, and ggplot2, ggpubr, and viridis for visualization. For α-diversity calculations, samples were rarefied to 11,449 sequence reads per sample. Differences in α-diversity between our metabolic measures of interest were assessed using generalized mixed-effects model analysis with participants used as the random effect variable and diet and sequence used as fixed effects. To measure β-diversity, samples were normalized by centred log-ratio transformation. Differences in β-diversity were assessed using permutational multivariate analysis of variance (PERMANOVA) assessing for differences by diet.

Metabolic data (including imaging data, blood chemistry, indirect calorimetry, and stable isotopes) are expressed as mean with 95% confidence interval or median with interquartile range. Analyses were performed in Prism (GraphPad; 9.0.2). Normality of data was assessed by the Shapiro-Wilk test. For normally distributed data, the effects of diets and cold on whole-body energy expenditure and substrate turnover as well as specific tissue composition and metabolism were assessed by a repeated measures ANOVA (if no missing values) or mixed-effects model (if missing values) with Bonferroni correction for multiple comparisons. Otherwise, for data that was not normally distributed, the Friedman test was used with Dunn's correction for multiple comparisons. Correlation and linear regression analyses were applied to investigate the relationships between BAT metabolic parameters and other metabolic and hormonal cofactors. The significance threshold was set at $p < 0.05$.

ADDITIONAL RESOURCES

ClinicalTrials.gov identifier NCT03188835.